

Stabilization of the fluidic pinball with gradient-enriched machine learning control

Guy Y. Cornejo Macea¹, Yiqing Li², François Lusseyran¹, Marek Morzyński³ and Bernd R. Noack^{2,4†}

¹Université Paris-Saclay, CNRS, LIMSI, 91400, Orsay, France.

²Center for Turbulence Control, Harbin Institute of Technology (Shenzhen), Room 312, Building C, University Town, Xili, Shenzhen 518058, People's Republic of China.

³Department of Virtual Engineering, Poznań University of Technology, Jana Pawla II 24, PL 60-965 Poznań, Poland.

⁴Institut für Strömungsmechanik und Technische Akustik (ISTA), Technische Universität Berlin, Müller-Breslau-Straße 8, D-10623 Berlin, Germany.

(Received xx; revised xx; accepted xx)

We stabilize the flow past a cluster of three rotating cylinders—the fluidic pinball—with automated gradient-enriched machine learning algorithms. The control laws command the rotation speed of each cylinder in an open- and closed-loop manner. These laws are optimized with respect to the average distance from the target steady solution in three successively richer search spaces. First, stabilization is pursued with steady symmetric forcing. Second, we allow for asymmetric steady forcing. And third, we determine an optimal feedback controller employing nine velocity probes downstream. As expected, the control performance increases with every generalization of the search space. Surprisingly, both open- and closed-loop optimal controllers include an asymmetric forcing, which surpasses symmetric forcing. Intriguingly, the best performance is achieved by a combination of phasor control and asymmetric steady forcing. We hypothesize that asymmetric forcing is typical for pitchfork bifurcated dynamics of nominally symmetric configurations. Key enablers are automated machine learning algorithms augmented with gradient search: explorative gradient method for the open-loop parameter optimization and a gradient-enriched machine learning control (gMLC) for the feedback optimization. gMLC learns the control law significantly faster than previously employed genetic programming control.

1. Introduction

We stabilize the wake behind a fluidic pinball using a hierarchy of model-free self-learning control methods from a one-parametric study of open-loop control to a gradient-enriched machine learning feedback control. Flow control is at the heart of many engineering applications. Traffic alone profits from flow control via drag reduction of transport vehicles (Choi *et al.* 2008), lift increase of wings (Semaan *et al.* 2016), mixing control for more efficient combustion (Dowling & Morgans 2005), and noise reduction (Jordan & Colonius 2013).

The control logic is a critical component for performance increases after the actuators and sensors have been deployed. The hardware is typically determined from engineering wisdom (Cattafesta & Shelpak 2011). The control law may be designed with a rich arsenal of mathematical methods. Control theory offers powerful methods for control

† Email address for correspondence: bernd.noack@hit.edu.cn

design with large success for model-based stabilization of low-Reynolds number flows or simple first and second order dynamics (Rowley & Williams 2006). Transport-related engineering applications are at high Reynolds numbers and thus associated with turbulent flows. So far, turbulence has eluded most attempts for model-based control albeit for few simple exceptions (Brunton & Noack 2015). Examples relate to first and second order dynamics, e.g., the quasi-steady response to quasi-steady actuation (Pfeiffer & King 2012), opposition control near walls (Choi *et al.* 1994; Fukagata & Nobuhide 2003), phasor control of oscillations (Pastoor *et al.* 2008) and two-frequency crosstalk (Glezer *et al.* 2005; Luchtenburg *et al.* 2009). In general, control design is challenged by the high-dimensionality of the dynamics, the nonlinearity with many frequency crosstalks, and the large time-delay between actuation and sensing.

Hence, most closed-loop control studies of turbulence resort to a model-free approach. A simple example is extremum seeking (Gelbert *et al.* 2012) for online tuning of one or few actuation parameters, like amplitude and frequency of periodic actuation. More complex examples involve high-dimensional parameter optimization with methods of machine learning, like evolutionary strategies (Koumoutsakos *et al.* 2001) and genetic algorithms (Benard *et al.* 2016). Even regression problems for nonlinear feedback laws have been learned by genetic programming (Ren *et al.* 2020) and reinforcement learning (Rabault *et al.* 2019).

Genetic programming control (GPC) has been pioneered by Dracopoulos (1997) over 20 years ago and has been proven to be particularly successful for nonlinear feedback turbulence control in experiments. Examples include the drag reduction of the Ahmed body (Li *et al.* 2018) and the same obstacle under yaw angle (Li *et al.* 2019), mixing layer control (Parezanović *et al.* 2016), separation control of a turbulent boundary layer (Debien *et al.* 2016), recirculation zone reduction behind a backward facing step (Gautier *et al.* 2015), and jet mixing enhancement (Zhou *et al.* 2020), just to name a few. GPC has consistently outperformed existing optimized control approaches, often with unexpected frequency crosstalk mechanisms (Noack 2019). GPC has a powerful capability to find new mechanisms (exploration) and populate the best minima (exploitation). Yet, the exploitation is inefficient leading to increasing redundant testing of similar control laws with poor convergence to the minimum. This challenge is well known and will be addressed in this study.

As benchmark control problem, we chose the fluidic pinball, the flow around three parallel cylinders one radius apart from each other (Noack *et al.* 2016; Deng *et al.* 2020; Chen *et al.* 2020). The triangle of centers points in the direction of the flow. The actuation is performed by rotating each cylinder independently. The flow is monitored by 9 velocity probes downstream. The control goal is the complete stabilization of the unstable symmetric steady Navier-Stokes solution. This choice is motivated by several reasons. First, already the unforced fluidic pinball shows a surprisingly rich dynamics. With increasing Reynolds number the steady wake becomes successively unstable in a Hopf bifurcation, a pitchfork bifurcation, another Hopf bifurcation before, eventually, a chaotic state is reached. Second, the cylinder rotations may encapsulate the most common wake stabilization approaches, like Coanda forcing (Geropp & Odenthal 2000), base bleed (Wood 1964; Bearman 1967), low-frequency forcing (Pastoor *et al.* 2008), high-frequency forcing (Thiria *et al.* 2006), phasor control (Roussopoulos 1993), and circulation control (Cortelessi *et al.* 1994). Third, the rich unforced and controlled dynamics mimics nonlinear behaviour of turbulence while the computation of the two-dimensional flow is manageable on workstations. To summarize, the fluidic pinball is an attractive all-weather plant for non-trivial multiple-input multiple-output control dynamics.

This study focusses on the stabilization of the unstable symmetric steady solution of

the fluidic pinball in the pitchfork regime, i.e., for asymmetric vortex shedding. This goal is pursued under symmetric steady actuation, general non-symmetric steady actuation and general nonlinear feedback control. We aim to physically explore the actuation mechanisms in a rich search space and to efficiently exploit the performance gains from gradient-based approaches. This multi-objective optimization leads to innovations of hitherto employed parameter optimizations and regression solvers as a beneficial side effect.

The manuscript is organized as follows. § 2 introduces the fluidic pinball problem and the corresponding direct numerical simulation. § 3 reviews and augments machine learning control strategies. In § 4, a hierarchy of increasingly more complex control laws is optimized for wake stabilization. § 5 summarizes the results and indicates directions for future research.

2. The fluidic pinball—A benchmark flow control problem

In this section, we describe the fluid system studied for the control optimization—the fluidic pinball. First we present the fluidic pinball configuration and the unsteady 2D Navier-Stokes solver in § 2.1, then the unforced flow spatio-temporal dynamics in § 2.2 and finally the control problem for the fluidic pinball in § 2.3.

2.1. Configuration and numerical solver

The test case is a two-dimensional uniform flow past a cluster of three cylinders of same diameter D . The center of the cylinders form an equilateral triangle pointing upstream. The flow is controlled by the independent rotation of the cylinders along their axis. The rotation of the cylinders enables the steering of incoming fluid particles, like a pinball machine. Thus, we refer this configuration as the fluidic pinball. In our study, we chose the side length of the equilateral triangle equal to be $1.5D$. The distance of one radius gives rise to an interesting flip-flopping dynamics (Chen *et al.* 2020).

The flow is described by a Cartesian coordinate system, where the origin is located midway between the two rearward cylinders. The x -axis is parallel to the streamwise direction and the y -axis is orthogonal to the cylinder axis. The velocity field is denoted by $\mathbf{u} = (u, v)$ and the pressure field by p . Here, u and v are, respectively, the streamwise and transverse components of the velocity. We consider a Newtonian fluid of constant density ρ and kinematic viscosity ν . For the direct numerical simulation, the unsteady incompressible viscous Navier-Stokes equations are non-dimensionalized with cylinder diameter D , the incoming velocity U_∞ and the fluid density ρ . The corresponding Reynolds number is $Re_D = U_\infty D / \nu$. Throughout this study, only $Re_D = 100$ is considered.

The computational domain Ω is a rectangle bounded by $[-6, 20] \times [-6, 6]$ and excludes the interior of the cylinders:

$$\Omega = \{[x, y]^\top \in \mathcal{R}^2 : [x, y]^\top \in [-6, 20] \times [-6, 6] \wedge (x - x_i)^2 + (y - y_i)^2 \geq 1/4, i = 1, 2, 3\}.$$

Here, $[x_i, y_i]^\top$ with $i = 1, 2, 3$, are the coordinates of the cylinder centers, starting from the front cylinder and numbered in mathematically positive direction,

$$\begin{aligned} x_1 &= -3/2 \cos(30^\circ) & y_1 &= 0, \\ x_2 &= 0 & y_2 &= -3/4, \\ x_3 &= 0 & y_3 &= 3/4. \end{aligned}$$

The computational domain Ω is discretized on an unstructured grid comprising 4225 triangles and 8633 nodes. The grid is optimized to provide a balance between computation

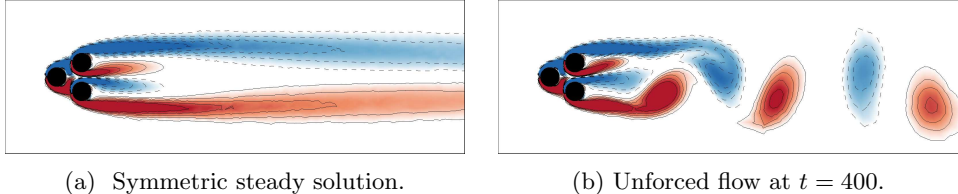


Figure 1: Vorticity fields for the unforced fluidic pinball at $Re_D = 100$. Blue (red) regions bounded by dashed lines represent negative (positive) vorticity. Darker regions indicate higher values of vorticity magnitude.

speed and accuracy. Grid independence of the direct Navier-Stokes solutions has been established by Deng *et al.* (2020).

The boundary conditions for the inflow, upper and lower boundaries are $U_\infty = \mathbf{e}_x$ while a stress-free condition is assumed for the outflow boundary. The control of the fluidic pinball is carried out by the rotation of the cylinders. A non-slip condition is adopted on the cylinders: the flow adopts the circumferential velocities of the front, bottom and top cylinder specified by $b_1 = U_F$, $b_2 = U_B$ and $b_3 = U_T$. The actuation command comprises these velocities, $\mathbf{b} = [b_1, b_2, b_3]^\top$. A positive (negative) value of the actuation command corresponds to counter-clockwise (clockwise) rotation of the cylinders along their axis. The numerical integration of the Navier-Stokes equations is carried by an in-house solver using a fully implicit Finite-Element Method (Noack *et al.* 2003, 2016). The method is third order accurate in time and space.

The initial condition for the numerical simulations is the symmetric steady solution. The symmetrical steady solution is computed with a Newton-Raphson method on the steady Navier-Stokes. An initial short small rotation of the front cylinder is used to kick-start the transient to natural vortex shedding in the first period (Deng *et al.* 2020). The transient regime lasts around 400 convective time units. Figure 1 shows the vorticity field for the symmetric steady solution and the natural unforced flow after 400 convective units. The snapshot at $t = 400$ in figure 1b will be the initial condition for all the following simulations.

2.2. Flow characteristics

The fluidic pinball is a geometrically simple configuration that comprises key features of real-life flows such as successive bifurcations and frequency crosstalk between modes. Deng *et al.* (2020) shows that the unforced fluidic pinball undergoes successive bifurcations with increasing Reynolds number before reaching a chaotic regime. The first Hopf bifurcation at Reynolds number $Re \approx 18$ breaks the symmetry in the flow and initiates the von Kármán vortex shedding. The second bifurcation at Reynolds number $Re \approx 68$ is of pitchfork type and gives rise to a transverse deflection of jet-like flow between the two rearward cylinders. The bi-stability of the jet deflection has been reported by Deng *et al.* (2020). At a Reynolds number $Re = 100$ the jet deflection is rapid and occurs before the vortex shedding is fully established. Figure 2a shows an increase of the lift coefficient C_L before oscillations set in and the lift coefficient converges against a periodic oscillation around a slightly reduced mean value. Those bifurcations are a consequence of multiple instabilities present in the flow: there are two shear instabilities, on the top and bottom cylinder, and a jet bi-stability originating from the gap between the two back cylinders. The shear-layer instabilities synchronize to von Kármán vortex shedding.

Figure 2 illustrates the dynamics of the unforced flow from the unstable steady symmetric solution to the post-transient periodic flow. The phase portrait in figure 2b

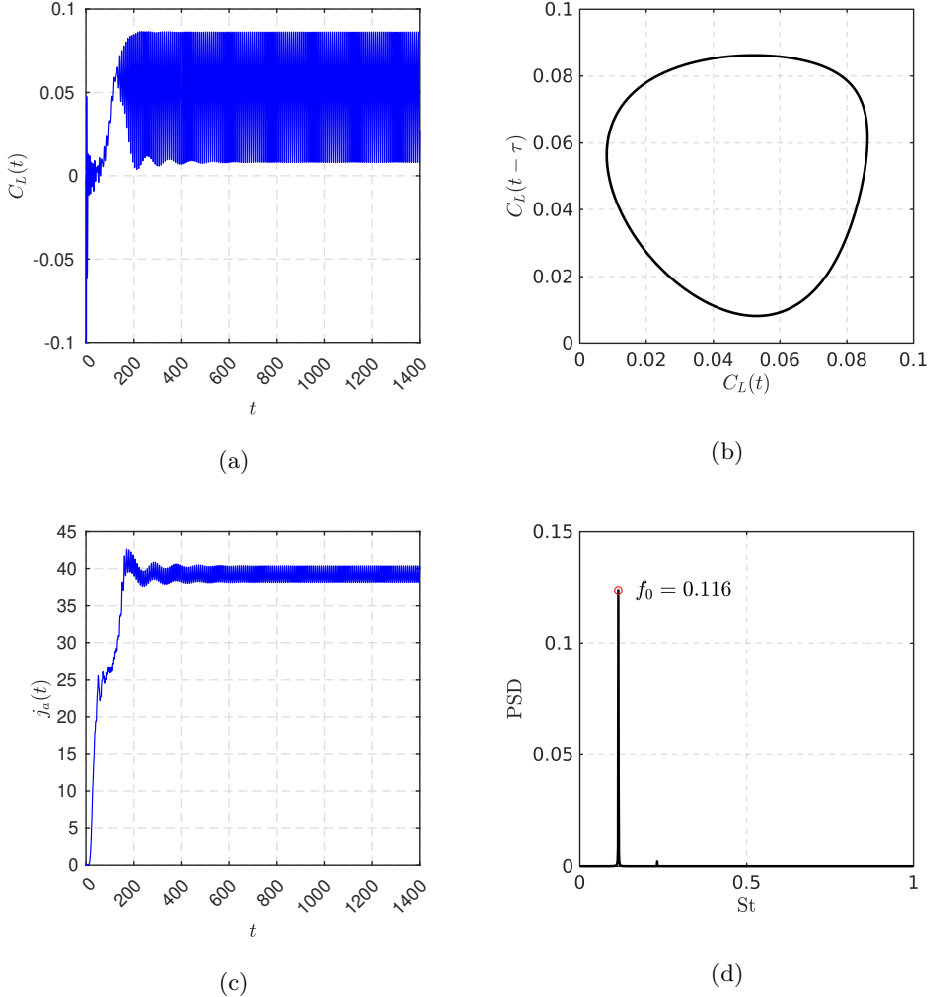


Figure 2: Characteristics of the unforced natural flow starting from the steady solution ($t = 0$). The transient spans until $t \approx 400$. (a) Time evolution of the lift coefficient C_L , (b) phase portrait, (c) time evolution of the instantaneous cost function j_a and (d) Power Spectral Density (PSD) showing the natural frequency $f_0 = 0.116$ and its first harmonic. The phase portrait is computed during the post-transient regime $t \in [900, 1400]$ and the PSD is computed over the last 1000 convective time units, $t \in [400, 1400]$.

and the power spectral density (PSD) in figure 2d show a periodic regime with frequency $f_0 = 0.116$ and its harmonic. Figure 2a shows that the mean value of the lift coefficient C_L is not null. This is due to the deflection of the jet behind the two rearward cylinders during the post-transient regime. During this regime, the deflection of the jet stays on one side as it is illustrated in figure 3a-3h over one period and in figure 3j in the mean field. This deflection explains the lift coefficient C_L asymmetry. Indeed, the upward oriented jet increases the pressure on the lower part of the top cylinder leading to an increase of the lift coefficient. In figure 2a, the initial downward spike on the lift coefficient is

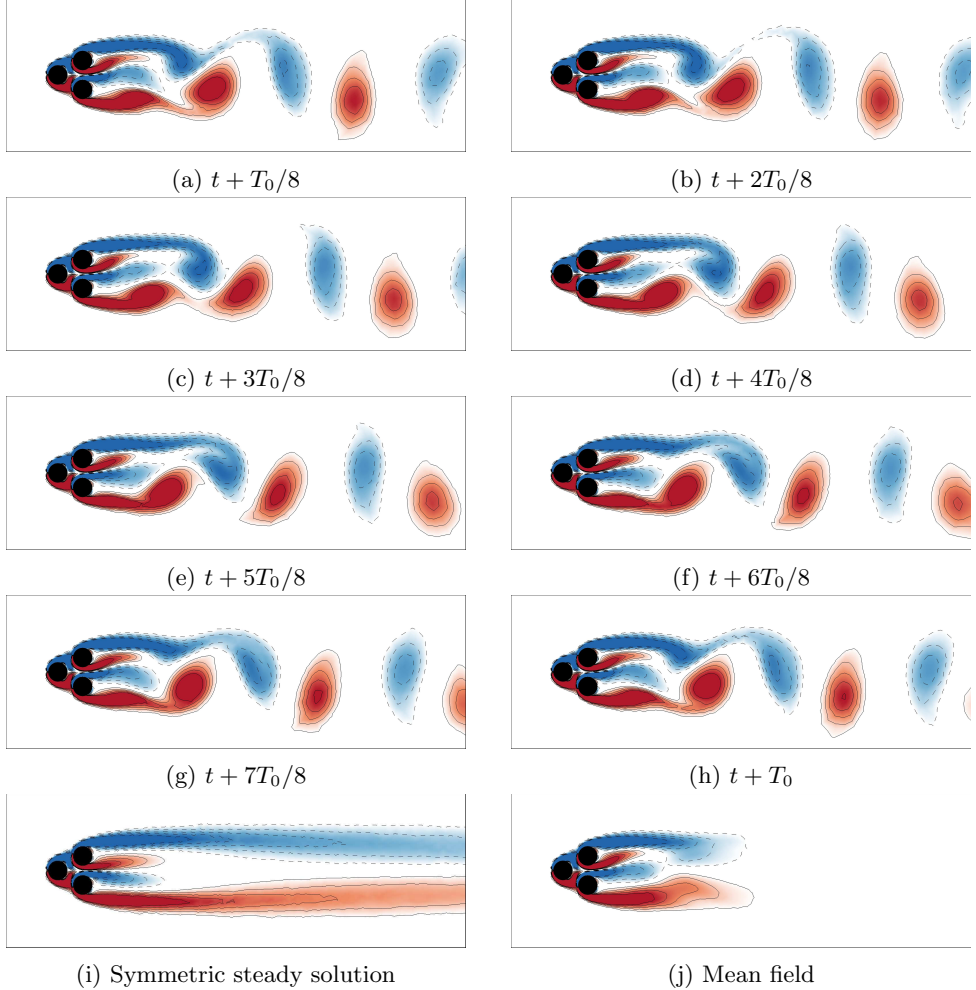


Figure 3: Vorticity fields of the unforced flow. (a)-(f) Time evolution of the vorticity field in the last period of the simulation, (i) the objective symmetric steady solution and (j) the mean field of the unforced flow. The color code is the same as figure 1. T_0 is the natural period associated to the natural frequency f_0 . The mean field has been computed by averaging the flow over 100 periods.

due to the initial kick. The unforced natural flow is our reference simulation for future comparisons.

Thanks to the rotation of the cylinders, the fluidic pinball is capable of reproducing six actuation mechanisms inspired from wake stabilization literature and exploiting distinct physics. Examples of those mechanisms can be found in Ishar *et al.* (2019). First, the wake can be stabilized by shaping the wake region more aerodynamically—also called fluidic boat tailing. Here, shear layer is vectored towards the center region with passive devices, like vanes (Flügel 1930) or active control through Coanda blowing (Geropp 1995; Geropp & Odenthal 2000; Barros *et al.* 2016). In the case of the fluidic pinball, we can mimic this effect by a counter-rotating rearward cylinders which accelerates the boundary layer and delays separation. This fluidic boat tailing is typically associated with significant drag reduction. Second, the two rearward cylinders can also rotate oppositely

ejecting a fluid jet on the centerline. Thus, interaction between the upper and lower shear layer is suppressed, preventing the development of a von Kármán vortex in the vicinity of the cylinders. Such base-bleeding mechanism has a similar physical effect as a splitter plate behind a bluff body and has been proved to be an effective means for wake stabilization (Wood 1964; Bearman 1967). Third, phasor control can be performed by estimating the oscillation phase and feeding it back with a phase shift and gain (Protas 2004). Fourth, unified rotation of the three cylinders in the same direction gives rise to higher velocities, and thus larger vorticity, on one side and the expense of the other side, destroying the vortex shedding. This effect relates to the Magnus effect and stagnation point control (Seifert 2012). Fifth, high-frequency forcing can be effected by symmetric periodic oscillation of the rearward cylinders. With a vigorous cylinder rotation (Thiria *et al.* 2006), the upper and lower shear layer are re-energized, reducing the transverse wake profile gradients and thus the instability of the flow. Thus, the effective eddy viscosity in the von Kármán vortices increases, adding a damping effect. Sixth and finally, a symmetrical forcing at a lower frequency than the natural vortex shedding may stabilize the wake (Pastoor *et al.* 2008). This is due to the mismatch between the anti-symmetric vortex shedding and the forced symmetric dynamics whose clock-work is distinctly out of sync with the shedding period. High- and low-frequency forcing lead to frequency crosstalk between actuation and vortex shedding over the mean flows, as described by low-dimensional generalized mean-field model (Luchtenburg *et al.* 2009).

The fluidic pinball is an interesting Multiple-Input Multiple-Output (MIMO) control benchmark. The configuration exhibits well-known wake stabilization mechanisms in physics. From a dynamical perspective, nonlinear frequency crosstalk can easily be enforced. In addition, even long-term simulations can easily be performed on a laptop within an hour.

2.3. Control objective and optimization problem

Several control objectives related to the suppression or reduction of undesired forces can be considered for the fluidic pinball. We can reduce the net drag power, increase the recirculation bubble length, reduce lift fluctuations or even mitigate the total fluctuation energy.

In this study, we aim to stabilize the unstable steady symmetric Navier-Stokes solution at $Re_D = 100$. The associated objectives are J_a , quantifying the closeness to the symmetric steady solution and J_b , the actuation power. The cost J_a is defined as the temporal average of the residual fluctuation energy of the actuated flow field \mathbf{u}_b with respect to the symmetric steady flow \mathbf{u}_s :

$$J_a = \frac{1}{T_{ev}} \int_{t_0}^{t_0+T_{ev}} j_a(t) dt \quad (2.1)$$

with the instantaneous cost function

$$j_a(t) = \|\mathbf{u}_b(t) - \mathbf{u}_s\|_{\Omega}^2 \quad (2.2)$$

based on the L_2 -norm

$$\|\mathbf{u}\|_{\Omega} = \sqrt{\iint_{\Omega} u^2 + v^2 dx}. \quad (2.3)$$

The control is activated at $t_0 = 400$ convective time units after the starting kick on the steady solution. Thus, we have a fully established post-transient regime. The cost function is evaluated until $T_{ev} = 1400$ convective time units. Thus, the time average

is effected over 1000 convective time units to make sure that the transient regime has far less weight as compared to the actuated regime. Yet, a faster stabilizing response to actuation is clearly desirable and factors positively into the cost.

J_b is naturally chosen as a measurement of the actuation energy investment. Evidently, a low actuation energy is desirable. The actuation power is computed as the power of the torque applied by the fluid on the cylinders. J_b is the time-averaged actuation power over $T_{ev} = 1000$ time units:

$$J_b(\mathbf{b}) = \frac{1}{T_{ev}} \int_{t_0}^{t_0+T_{ev}} \sum_{i=1}^3 \mathcal{P}_{act,i} dt \quad (2.4)$$

where $\mathcal{P}_{act,i}$ is the actuation power supplied integrated over cylinder i :

$$\mathcal{P}_{act,i} = - \oint b_i F_{si}^\theta ds$$

where $(F_{si}^\theta ds)$ is the azimuthal component of the local fluid forces applied to cylinder i . The negative sign denotes that the power is supplied and not received by the cylinders.

In this study, optimization is based on the cost function $J = J_a$ and the actuation investment J_b is evaluated separately. We refrain from a cost function J which employs the objective function J_a and penalizes the actuation investment J_b with suitable weight γ , i.e., $J = J_a + \gamma J_b$. The procedure has two reasons. First, the distance between two flows and actuation energy belong to two different worlds, kinematics and dynamics. Any choice of the penalization parameter γ will be subjective and implicate a sensitivity discussion. Second, the complete stabilization of the steady solution would lead to a vanishing actuation $\mathbf{b} \equiv 0$ and thus vanishing energy J_b . Thus, the optimization problem without actuation energy can be expected to be well-posed.

The instantaneous cost function j_a of the unforced flow is shown in figure 2c. We notice a slight overshoot around $t = 200$ before converging to a post-transient fluctuating regime. The post-transient regime shows the expected periodic behaviour from von Kármán vortex shedding. The cost averaged over 1000 convective time units is $J_0 = 39.08$ and serves as reference to actuation success.

To reach the steady symmetric solution, the flow is controlled by the rotation of the three cylinders. The actuation command $\mathbf{b} = [b_1, b_2, b_3]^\top$ is determined by control law \mathbf{K} . This control law may operate open-loop or closed-loop with flow input. Considered open-loop forcings are steady or harmonic oscillation around a vanishing mean. Considered feedback includes velocity sensor signals in the wake. Thus, in the most general formulation, the control law reads

$$\mathbf{b}(t) = \mathbf{K}(\mathbf{h}(t), \mathbf{s}(t)) \quad (2.5)$$

with $\mathbf{h}(t)$ and $\mathbf{s}(t)$ being vectors comprising respectively time dependent harmonic functions and sensor signals. The sensor signals include the instantaneous velocity signals as well as three recorded values over one period as elaborated in the result section § 4.3. In the following, N_b represents the number of actuators, N_h for the number of time-dependent functions and N_s for the number of sensor signals. Then optimal control problem determines the control law which minimizes the cost:

$$\mathbf{K}^* = \arg \min_{\mathbf{K} \in \mathcal{K}} J(\mathbf{K}) \quad (2.6)$$

with $\mathcal{K} : X \mapsto Y$ being the space of control laws. Here, X is the input space, e.g., sensor signals and Y is the output for actuation commands. In general, (2.6) is a challenging non-convex optimization problem.

3. Control optimization framework

In this section, we present the control optimization for stabilizing the fluidic pinball. This constitutes a challenging nonlinear non-convex optimization problem in which the possibility of several local minima must be expected. Hence, we specifically address how to explore new minima while keeping the convergence rate and efficiency of gradient-based approaches. In § 3.1, the principles of exploration and exploitation are discussed for parameter and control law optimization. Then, the employed algorithms are described: the Explorative Gradient Method (EGM) for parametric optimization (§ 3.2) and the gradient-enriched Machine Learning Control (gMLC) for control law optimization (§ 3.3).

3.1. Optimization principles—Exploration versus exploitation

The two algorithms, EGM and gMLC, enable model-free control optimization. These algorithms combine the advantages of exploitation and exploration. Exploitation is based on a downhill simplex method with the best performing of all tested control laws, also called ‘individuals’. The goal is to ‘slide down’ the best identified minimum.

Exploration is performed with another algorithm using all previously tested individuals. The goal is to find potentially new and better minima, ideally the global minimum. The method for exploration depends on the search space. For a low-dimensional parameter space, a space-filling version of the Latin Hypercube Sampling (LHS) guarantees optimal geometric coverage of the search space. For a high-dimensional function space, genetic programming is found to be efficient.

EGM and gMLC start with an initial set of individuals to be evaluated. Then, exploitative and explorative phases iterate until a convergence criterion is reached. The iteration hedges against several worst-case scenarios. The control landscape may have only a single minimum accessible from any other point by steepest descend. In this case, exploration is often inefficient, although it might help in avoiding slow marches through long shallow valleys (Li *et al.* 2020*b*). The control landscape may also have many minima accessible by gradient-based searches. In this case, exploitation is likely to incrementally improve performance in suboptimal minima and the search strategy should have a significant investment in exploration. The minima of the control landscape may also have narrow basins of attractions for gradient-based iterations and extended plateaus. This is another scenario where iteration between exploitation and exploration is advised.

Many optimizers balance exploration and exploitation and gradually shift from the former to the latter. This strategy sounds reasoning but is not a good hedge against the described worst case scenarios where almost all exploitative or almost all explorative algorithms are doomed to fail.

Note that the chances of exploration landing close to a new better minimum are small. Yet, the explorative phases may find new basins of attractions for successful gradient-based descends. This is another argument for the alternating execution of exploration and exploitation.

Finally, we note that the proposed explorative-exploitive schemes allows that both kinds of iterations may be adjusted to the control landscape. For instance, LHS in a high-dimensional search space will initially explore only the boundary and may better be replaced by Monte-Carlo or a genetic algorithm. We refer to Li *et al.* (2020*b*) for a thorough comparison of EGM and five common optimizers and to Duriez *et al.* (2016) for genetic programming control. The next two sections detail both optimizers, EGM and gMLC.

3.2. Parameter optimization with the explorative gradient method

The Explorative Gradient Method (EGM) optimizes N_p parameters $\mathbf{b} = [b_1, \dots, b_{N_p}]^\top$ with respect to cost $J(\mathbf{b})$ and comprises exploration and exploitation phases. In the parameter optimization, we do not differentiate between the control law $\mathbf{K} = \text{const}$ and the associated actuation command $\mathbf{b} = \mathbf{K}$. The search space, or actuation domain, is a compact subset \mathcal{B} of \mathbb{R}^{N_p} , typically defined by upper and lower bounds for each parameter. The exploration phase is based on a space-filling variant of Latin hypercube sampling (LHS) (McKay *et al.* 1979) whereas the exploitation phase is carried out by Nelder-Mead's *downhill simplex* (Nelder & Mead 1965).

The first $N_p + 1$ initial individuals \mathbf{b}_m , $m = 1, \dots, N_p + 1$ define the first ‘amoeba’ of the downhill simplex method. The first individual \mathbf{b}_1 is typically placed at the center of \mathcal{B} . The N_p remaining vertices are slightly displaced along the b_m axes. In other words, $\mathbf{b}_m = \mathbf{b}_1 + h_m \mathbf{e}_{m-1}$ for $m = 2, \dots, N_p + 1$. Here, $\mathbf{e}_m := [\delta_{m,1}, \dots, \delta_{m,N_p}]^\top$ is the unit vector in the m th direction and h_m is the corresponding step size. The increment h_m is chosen to be small compared to the range of the corresponding dimension.

The exploitation phase employs the downhill simplex method. This method is robust and widely used for data-driven optimization in low and moderate-dimensional search spaces. No analytical cost function and no local gradients are required. The new individual is a linear combination of the simplex individuals and follows a geometric reasoning. The vertex with the worst performance is replaced by a point reflected at the centroid of the opposite side of the simplex. This step leads to a mirror-symmetric version of the simplex where the new vertex has the best performance if the cost function depends linearly on the input. Subsequent operations, like expansion, single contraction, and global shrinking ensure that iterations exploit a favourable downhill behaviour and avoid getting stuck by nonlinearities. We refer to Li *et al.* (2020b) for a detailed description.

The explorative phase of EGM is inspired by the LHS method. LHS aims to fill the complete domain \mathcal{B} optimally. The pre-defined number m of parameters maximizes the minimum distance of its neighbours:

$$\{\mathbf{b}_1^{\text{LHS}}, \dots, \mathbf{b}_m^{\text{LHS}}\} := \arg \max_{\mathbf{b}_1, \dots, \mathbf{b}_m \in \mathcal{B}} \min_{\substack{i \in \{1, \dots, m-1\}, \\ j \in \{i+1, \dots, m\}}} \|\mathbf{b}_i - \mathbf{b}_j\|.$$

Here, $\|\cdot\|$ denotes the Euclidean norm. The number of individuals has to be determined in advance and cannot be augmented. This static feature is incompatible with the iterative EGM algorithm. We resort to a recursive ‘greedy’ version. Let \mathbf{b}_1^\bullet be the first parameter. Then, \mathbf{b}_2^\bullet maximizes the distance from \mathbf{b}_1^\bullet ,

$$\mathbf{b}_2^\bullet := \arg \max_{\mathbf{b} \in \mathcal{B}} \|\mathbf{b} - \mathbf{b}_1^\bullet\|.$$

The m th parameter maximizes the minimum distance to all previous individuals,

$$\mathbf{b}_m^\bullet := \arg \max_{\mathbf{b} \in \mathcal{B}} \min_{i \in \{1, \dots, m-1\}} \|\mathbf{b} - \mathbf{b}_i^\bullet\|.$$

This recursive definition allows adding explorative phases from any given set of individuals.

Exploitation and exploration are iteratively continued until the stopping criterion is reached. The stopping criterion may be a total number of cost function evaluations, a threshold value for improvements. The *Explorative Gradient Method* (EGM) phases are summarized in algorithm 1.

Algorithm 1: Explorative Gradient Method

Result: \mathbf{b}^* , the best individual

Initialize the $N_p + 1$ individuals of the dataset \mathcal{B}_I ;

Test all the individuals;

Build the simplex \mathcal{S} by taking the $N_p + 1$ best individuals;

while Stopping criterion is not reached **do**

- Exploration phase—Latin hypercube sampling**
 - Select \mathbf{b}^{LHS} by solving:
$$\mathbf{b}^{\text{LHS}} := \arg \max_{\mathbf{b} \in \mathcal{B}} \min_{\mathbf{b}_i \in \mathcal{B}_I} \|\mathbf{b} - \mathbf{b}_i\|$$
 - Test \mathbf{b}^{LHS} ;
 - Augment dataset: $\mathcal{B}_I := \mathcal{B}_I \cup \{\mathbf{b}_{\text{LHS}}\}$;
 - Update simplex: replace the worst individual of \mathcal{S} by \mathbf{b}^{LHS} ;
- end**
- Exploitation phase—Downhill simplex**
 - Sort and relabel \mathcal{S} such as: $J_1^S \leq J_2^S \leq \dots \leq J_{N_p+1}^S$;
 - Compute the centroid $\mathbf{c} = \frac{1}{N_p} \sum_{i=1}^{N_p} \mathbf{b}_i$ of \mathcal{S} excluding \mathbf{b}_{N_p+1} ;
 - Reflection:** compute and test $\mathbf{b}_r := \mathbf{c} + (\mathbf{c} - \mathbf{b}_{N_p+1})$;
 - if** $J_1^S < J_r^S < J_{N_p+1}^S$ **then**
 - Update simplex: $\mathbf{b}_{N_p+1} := \mathbf{b}_r$;
 - else if** $J_r^S < J_1^S$ **then**
 - Expansion:** compute and test $\mathbf{b}_e := \mathbf{c} + 2(\mathbf{c} - \mathbf{b}_{N_p+1})$;
 - Update simplex: $\mathbf{b}_{N_p+1} := \min\{\mathbf{b}_r, \mathbf{b}_e\}$;
 - else if** $J_{N_p+1}^S \leq J_r^S$ **then**
 - Contraction:** compute and test $\mathbf{b}_c := 1/2(\mathbf{c} + \mathbf{b}_{N_p+1})$;
 - if** $J_c^S < J_{N_p+1}^S$ **then**
 - Update simplex: $\mathbf{b}_{N_p+1} := \mathbf{b}_c$;
 - else**
 - Shrink:** compute and test $\mathbf{b}_{s,i} := 1/2(\mathbf{b}_1 + \mathbf{b}_i)$, $i = 2, \dots, N_p + 1$;
 - Update simplex: $\mathbf{b}_i := \mathbf{b}_{s,i}$, $i = 2, \dots, N_p + 1$;
 - end**
 - end**
 - Augment dataset: add all the new individuals to \mathcal{B}_I ;
- end**

3.3. Multiple-input multiple-output control optimization with gradient-enriched machine learning control

In this section, we cure a challenge of linear genetic programming control—the sub-optimal exploitation of gradient information. Starting point is machine learning control (MLC) based on linear genetic programming (LGP). MLC optimizes a control law without assuming a polynomial or other structure of the mapping from input to output. The only assumption is that the law can be expressed by a finite number of mathematical operations with a finite memory, i.e., is computable. The optimization process relies on a stochastic recombination of the control laws, also called *evolution*. MLC has been amazingly efficient in outperforming existing optimal control laws—often

with surprising frequency crosstalk mechanisms—in dozens of experiments (Noack 2019). MLC demonstrates a good exploration of actuation mechanisms but a slow convergence to an optimum despite an increasing testing of redundant similar control laws.

The proposed gradient-enriched MLC departs in two aspects from MLC. First, the concept of evolution from generation to generation is not adopted. The genetic operations include *all* tested individuals. One can argue that the neglection of previous generations might imply loss of important information. Second, the exploitation is accelerated by downhill subplex iteration (Rowan 1990). The best $k+1$ individuals are chosen to define a k -dimensional subspace and a downhill simplex algorithm optimizes the control law in this subspace.

MLC and gMLC share a representation of the control laws used for LGP (Brameier & Banzhaf 2006). The individuals are considered as little computer programs, using a finite number N_{inst} of instructions, a given register of variables and a set of constants. The instructions employ basic operations ($+$, $-$, \times , \div , \cos , \sin , \tanh , etc.) using inputs (h_i time-dependent functions and s_i sensor signals) and yielding the control commands as outputs. A matrix representation conveniently comprises the operations of each individual. Every row describes one instruction. The first two columns define the register indices of the arguments, the third column the index of the operation and the fourth column the output register. Before execution, all registers are zeroed. Then, the first registers are initialized with the input arguments, while the output is read from the last registers after the execution of all instructions. This leads to a $N_{\text{inst}} \times 4$ matrix representing the control law \mathbf{K} . We refer to Li *et al.* (2018) for details.

The algorithm begins with a Monte Carlo initialization of N_{MC} individuals, i.e., the indices of the matrix. The cost of these randomly generated functions are evaluated in the plant. The number of individuals N_{MC} needs to balance exploration and cost. Too few individuals may lead to descend in a suboptimal local minimum. Too many individuals may lead to unnecessary inefficient testing, as Monte Carlo sampling is purely explorative.

Once the initial individuals are evaluated, an exploration phase is carried out. New individuals are generated thanks to crossover and mutation operations. Thus, this phase is also referred as evolution phase. These operations are performed on the matrix representation of the individuals. As for MLC, crossover combines two individuals by exchanging lines in their matrix representation, whereas mutation randomly replaces values of some lines by new ones. In this approach, as we no longer consider a population but the database of all the individuals evaluated so far. Thus, we no longer need the replication and elitism operators of MLC. This choice is justified by the fact that we want to learn as much as possible from what we already know and avoid reevaluating individuals. To perform the crossover and mutation operation, individuals are selected from the database thanks to a tournament selection. A tournament selection of size 7 for a population of 100 individuals is used in Duriez *et al.* (2016). That means that for a population of 100 individuals, 7 individuals are selected randomly and the among the 7, the best one is chosen for the crossover or mutation operation. For gMLC, as the individuals are selected among all the evaluated individuals, the tournament size is properly scaled at each call to preserve the 7/100 ratio between the tournament size and the size of the database. The crossover and mutation operation are repeated randomly following P_c , the crossover probability, and P_m , the mutation probability, until N_G individuals are generated. The probabilities P_c and P_m are such as $P_m + P_c = 1$.

Once the evolution phase is achieved, N_G new individuals are generated thanks to downhill subplex iterations. Being in an infinite dimension function space, Nelder-Mead's downhill simplex is impractical as an exploitation tool. Thus, we propose a variant of downhill simplex inspired by Rowan (1990), commonly called *downhill subplex*. Just as

downhill simplex, the strength of this approach is to exploit local gradients to explore the search space. In the original approach of Rowan (1990), downhill simplex is applied to several orthogonal subspaces. However, in order to limit the number of cost function evaluations, we apply downhill simplex to only one subspace. This subspace is initialized by selecting N_{sub} individuals. Two ways to build the subspace after the Monte Carlo process are listed below:

- **Choose only the best individual:** select the best N_{sub} individuals evaluated so-far in the whole database.
- **Individuals near a minimum:** select the best individual evaluated so-far and the $N_{\text{sub}} - 1$ individuals closest to the best one.

The first approach has the benefit to comprise several minima candidates, whereas the second one is bound to lead to a minimum in the neighborhood of the best individual and relies on a given metric. Once the subspace is built, the next steps are similar to the downhill simplex method. As subplex and simplex are essentially the same algorithm applied to different spaces, we will not designate them differently.

Following the situation, downhill subplex may call 1 (only replication), 2 (expansion or single contraction) or $N_{\text{sub}} + 1$ (shrink) times the cost function. Several iterations of downhill subplex are repeated until at least N_G individuals are generated. In this study, the same number of individuals generated with the evolution phase and the downhill subplex phase is chosen to balance exploration and exploitation.

If the stopping criterion is reached, the most efficient individual in the database is given back. Otherwise, we restart a new cycle by generating new individuals with a new evolution phase, combining and modifying individuals derived by evolution and downhill subplex. However, the individuals built thanks to downhill subplex are linear combination of the original N_{sub} individuals. These new individuals do not have a matrix representation which is necessary to generate new individuals with genetic operators in the exploitation phase. To overcome this problem, we introduce a new phase to compute a matrix representation for the linearly-combined control laws. The matrix representation is computed by solving a regression problem of the first kind, similar to a function fitting problem, for all the linearly-combined control laws. First, each control law \mathbf{K}_i is evaluated on randomly sampled inputs \mathbf{s}_{rand} . The resulting output $\mathbf{K}_i(\mathbf{s}_{\text{rand}})$ is used to solve a secondary optimization problem:

$$\mathbf{K}_M^* = \arg \min_{\mathbf{K}_M} \|(\mathbf{K}_M(\mathbf{s}_{\text{rand}}) - \mathbf{K}_i(\mathbf{s}_{\text{rand}}))\|^2 \quad (3.1)$$

where $\|\cdot\|$ denotes the Euclidean norm. This optimization problem is a function fitting problem that we solve with linear genetic programming. The LGP parameters are the same used for the gMLC so the computed individuals are compatible with the ones in the database. The best fitting control law \mathbf{K}_M^* has then a matrix representation and is used as a substitute for the original linear combination of control laws. The substitutes are then used for the evolution phase even though they may not be perfect substitutes of the original control laws. Indeed, following the stopping criterion and population size of the secondary LGP optimization, the control law substitutes may not be able to reproduce all the characteristics of the linearly-combined control laws. An accurate but costly representation may not be needed as the control laws will be recombined afterwards. Moreover, the introduction of some error may be beneficial to improve the exploration phase and enrich our database.

Once the matrix representations are computed, a new cycle may begin with a new evolution phase. In this phase, if any individual has a better performance than the N_{sub} individuals in the simplex, then the least performing individuals among the N_{sub}

individuals are replaced. Thus, each evolution phase replaces elements in the simplex, allowing exploration beyond the initial subspace. Then, the optimization continues with the exploitation phase on the updated N_{sub} individuals.

Algorithm 2: Gradient-enriched Machine Learning Control

Result: \mathbf{K}^* , the best individual

Monte Carlo initialization: generate N_{MC} individuals;

Test all the individuals;

Build the subplex \mathcal{S} by taking the N_{sub} best individuals;

while Stopping criterion is not reached **do**

Exploration phase—Evolution

Generate and test N_G individuals from all the individuals evaluated so far thanks to crossover and mutation;

Update subplex \mathcal{S} : choose the N_{sub} best individuals among the new N_G individuals and the N_{sub} subplex individuals;

end

Exploitation phase—Downhill subplex

while The number of subplex individuals generated < N_G **do**

Perform a downhill subplex iteration in the subspace spanned by linear combinations of N_{sub} subplex control laws
(Downhill simplex method like in algorithm 1);

end

Reconstruction phase—Linear genetic programming

Compute a matrix representation for each new downhill subplex individual
(replace linearly-combined individuals by matrices using LGP);

end

end

Figure 4 illustrates the initialization, exploration and exploitation of gMLC. The exploration is based on LGP. Also the exploitation requires LGP. In the downhill simplex method, the individuals are linear combinations of the subplex basis and are finally approximated as matrices. This process is repeated until the stopping criterion is reached. The *Gradient-enriched Machine Learning Control (gMLC)* is summarized by pseudo code in algorithm 2.

Finally, figure 5 summarizes the exploration and exploitation phases for EGM and gMLC.

4. Flow stabilization

In this section, we stabilize the fluidic pinball with optimized control laws in increasingly more general search spaces. First (§ 4.1), we consider symmetric steady actuation with a parametric study reduced to one parameter $b_2 = -b_3 = \text{const}$. Then (§ 4.2), we optimize steady actuation allowing also for non-symmetric forcing, i.e., 3 independent inputs b_1, b_2, b_3 . Finally (§ 4.3), we optimize sensor-based feedback from 9 downstream sensor signals driving the 3 cylinder rotations. Evidently, the three search spaces are successive generalizations.

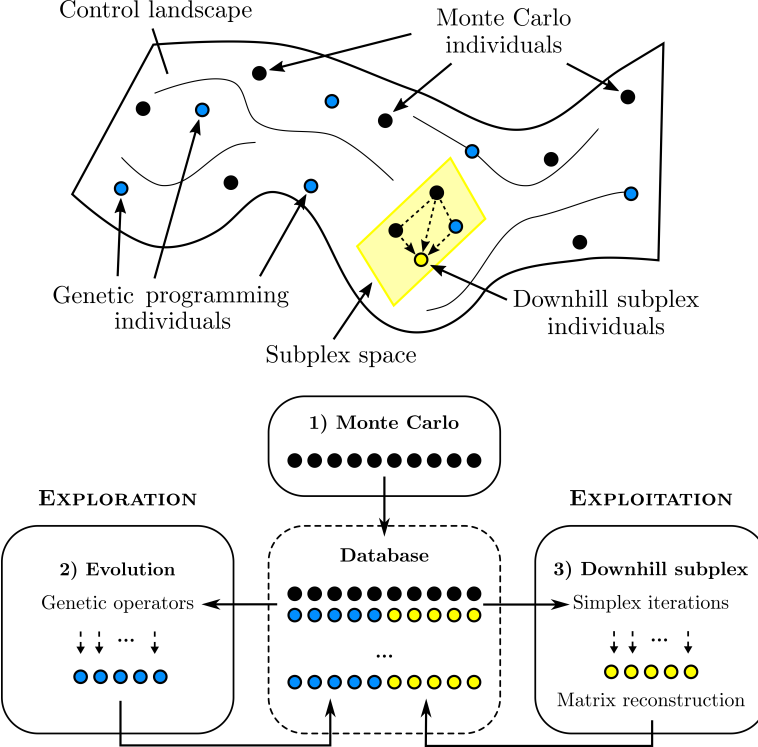


Figure 4: Schematic of the gradient-enriched MLC algorithm (bottom) and distribution of individuals in the search space (top). First (1), Monte Carlo initialization performs a first coarse exploration of the search space. Second (2), further exploration is performed thanks to genetic programming. Individuals are selected in the whole dataset and combined thanks to genetic operators to generate new individuals (blue dots). Then the database is augmented with the new individuals. Third (3), exploitation focuses on a subspace (represented in yellow) of finite dimension where downhill simplex iterations builds new individuals by linear combination (yellow dots). A matrix representation is computed for the downhill subplex individuals thanks to linear genetic programming , allowing the downhill subplex individuals to be included in the database.

4.1. Symmetric steady actuation—Parametric study

This section describes the behaviour of the fluidic pinball under a symmetric steady actuation. In this configuration, only the two rearward cylinders rotate at equal but opposite rotation speeds, $b_2 = -b_3$. When b_2 is positive, the rearward cylinders accelerate the outer boundary layers and suck near-wake fluid upstream. This forcing delays separation, mimics Coanda forcing and leads to a fluidic boat tailing. When b_2 is negative, the cylinders eject fluid in the near wake like in base bleed and oppose the outer boundary-layer velocities. Figure 6 shows the evolution of J_a/J_0 (top), J_b (middle) and the bifurcation diagram (bottom) as a function of b_2 .

We limited our study to $b_2 \in [-5, 6]$. The trends are resolved with a discretization step of 0.25 and a finer resolution in the ranges $[-2.5, 0]$ and $[1, 2]$. For each parameter, the cost J_a and actuation power J_b have been computed over 1000 convective time units. The bifurcation diagram has been built by detecting the extrema of the lift coefficient over the last 600 convective time units. The bifurcation diagram reveals five regimes:

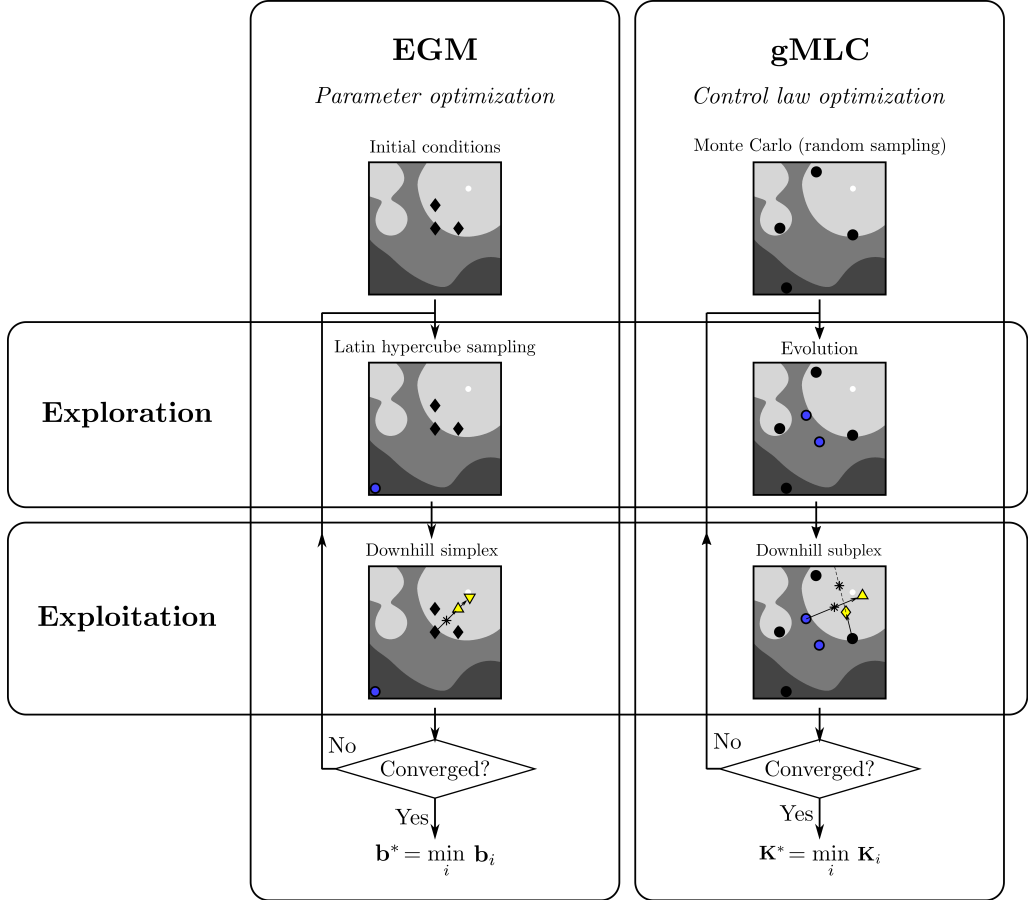


Figure 5: Summary of the explorative gradient method (EGM) (left column) and gradient-enriched machine learning control (gMLC) (right column). The level plots are a schematic representation of the control landscape. Darker regions depict poor performances and light regions depict good performances. Three minima are shown, two on the top left and one in the top right. The global minimum is depicted by a white dot in the top left region. The map represents an affine space (of finite dimension) for EGM and a Hilbert function space for gMLC. The initialization step is depicted with black diamonds for EGM and black dots for gMLC. The individuals generated thanks to an exploration phase are represented by blue dots. Exploration is carried out with LHS for EGM and evolution with genetic operators (crossover and mutation) for gMLC. The individuals generated thanks to an exploitation phase are represented in yellow. For EGM, downhill simplex steps are carried out. The associated level plot depicts one iteration of downhill simplex: the reflected individual (yellow triangle) and the expanded individual (reversed yellow triangle), the star is the centroid of the two best black diamonds. For gMLC, the simplex steps are carried out in a subspace (downhill subplex) of finite dimension. The associated level plot depicts two distinct simplex steps: first, a reflection step (yellow triangle) with the two best black dots and the best blue dot; then a contraction step (yellow diamond) with the same black dots and the newly evaluated yellow triangle. The stars are the centroids for each step. This process is repeated until the stopping criterion is reached. In this figure, only one iteration of the loop is depicted. The reconstruction phase is not depicted for the sake of clarity.

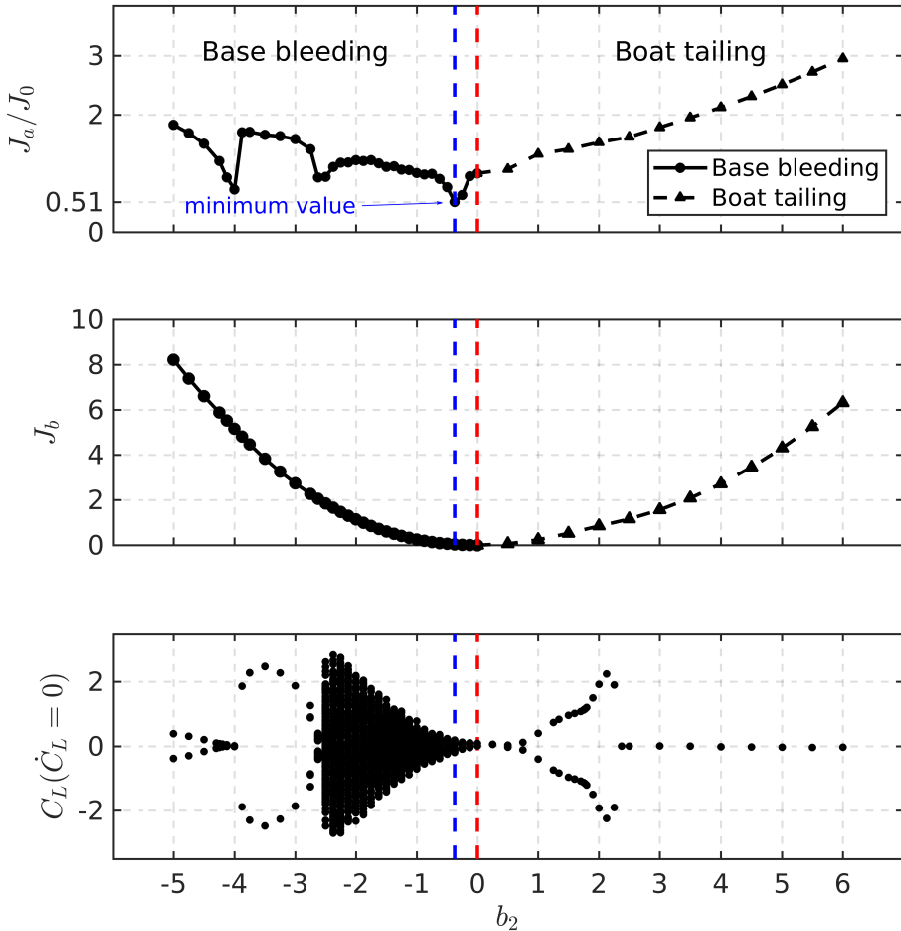


Figure 6: Parametric study for symmetric steady forcing. $b_2 = -b_3$ is the velocity of the bottom cylinder. The normalized distance to the steady solution J_a/J_0 (top) and the actuation power J_b (middle) are plotted as a function of b_2 . The bifurcation diagram (bottom) comprises all local maximum and minimum lift values. The vertical red dashed line corresponds to $b_2 = 0$ and separates the base bleeding and the boat tailing configurations. The global minimum of J_a/J_0 is reached at $b_2 = -0.375$, as indicated by a vertical blue dashed line.

Regime $b_2 < -4$: the lift amplitude decreases to zero and the cost decreases to the first minimum.

Regime $-4 < b_2 < -2.5$: the extremal lift values increase and decrease to zero again. The cost approaches another local minimum near $b \approx -2.5$.

Regime $-2.54 < b_2 < 0$: a period doubling cascade is observed for decreasing b_2 leading to a chaotic regime. At $b_2 \approx 0.375$, the cost assumes its global minimum with residual fluctuation of the lift coefficient.

Regime $0 < b_2 < 2.375$: the cost and the extremal lift values monotonically increase.

Regime $2.375 < b_2$: the Coanda forcing completely stabilizes a symmetric steady solution. The cost increases with the rotation speed.

Interestingly, the boat tailing discontinuity at $b_2 = 2.375$ does not appear in the graph of the cost function J_a/J_0 . This continuity, even in the derivative, corresponds to a continuous passage from a periodic symmetrical solution to a stationary solution which is itself symmetrical. As the value of the cost function indicates, this stationary solution is quite far from the unforced symmetric steady solution. The global minimum of $J_a/J_0 = 0.51$ is reached near $b_2 = -0.375$, i.e., for a base bleeding configuration, corresponding to a small actuation power $J_b = 0.0315$, roughly 0.1% of the J_0 .

The characteristics of the best base bleeding solution leading closest to the symmetric steady solution are depicted in figure 7. In figure 7a, the lift coefficient is displayed for the unforced transient (blue curve) and the forced flow (red curve). The unforced flow terminates in an asymmetric shedding with positive lift values. After the start of forcing, the lift coefficient oscillates vigorously around its vanishing mean value. This forced statistical symmetry is corroborated by the oscillating jet in figures 8a-8h. Base bleed increases the velocity of the rearward jet compared to the unforced flow. This jet instability mitigates the Coanda effect on the bottom and top cylinder, i.e., the jet neither stays long at either side.

The vortex shedding persists similar to the unforced flow. However, the dominant frequency is increase from $f_0 = 0.116$ to $f_1 = 0.138$. The instantaneous cost function j_a in figure 7c shows an unsteady non-periodic behavior, reaching intermittently low levels. The broad spectral peak in figure 7d is a characteristic of a chaotic regime. The phase portrait in figure 7b corroborates the non-periodic oscillatory behaviour. The mean field in figure 8j, shows that actuated mean jet is symmetric unlike the mean field of the unforced flow. Moreover, the shear-layer on the upper and lower sides extend further downstream as compared to the unforced state.

This parametric study reveals that base bleeding is the best symmetric steady forcing strategy to bring the flow close to the symmetric steady solution. However, even though the cost J_a/J_0 is almost halved, the best base bleeding control fails to stabilize the flow.

4.2. General non-symmetric steady actuation—Explorative gradient method

In this section we aim to stabilize the symmetric steady solution by commanding the three cylinders with constant actuation without symmetry constraint. This three-dimensional parameter space is explored with the explorative gradient method presented in section § 3.2. The symmetry along the x -axis of the fluidic pinball allow us to reduce our search space and to explore only positive values of b_1 . A coarse initial parametric study carried on b_1 , b_2 and b_3 by steps of unity indicates that the global minimum of J_a/J_0 should be near $[b_1, b_2, b_3]^\top = [1, 0, 0]^\top$. Thus, we limit our research to the actuation domain $\mathcal{B} = [0, 2] \times [-2, 2] \times [-2, 2]$. The limitation of b_1 to positive values exploits the mirror symmetry of the configuration. Figure 9 (bottom) depicts the cost function in the actuation domain \mathcal{B} . Three planes ($b_1 = \text{const}$) are computed by interpolating parameters on a coarse grid. The individuals computed with EGM are all shown in the 3D space. The four initial control laws for EGM are the center of the box and shifted points from this center. The shift is 10% of the box size in positive coordinate direction. Thus, the four initial control laws are: $[1, 0, 0]^\top$, $[1.2, 0, 0]^\top$, $[1, 0.4, 0]^\top$ and $[1, 0, 0.4]^\top$. The exploration phase is performed in \mathcal{B} . For algorithmic reasons, the explorative points are chosen from 1 million points obtained from a space filling LHS. On one hand, we notice that the exploration phases (LHS in blue) focus on the boundary of the search space. This is consistent with the definition of LHS, as the furthest initial individuals are on the boundary of the box. On the other hand, the exploitation phases (simplex in yellow) stay

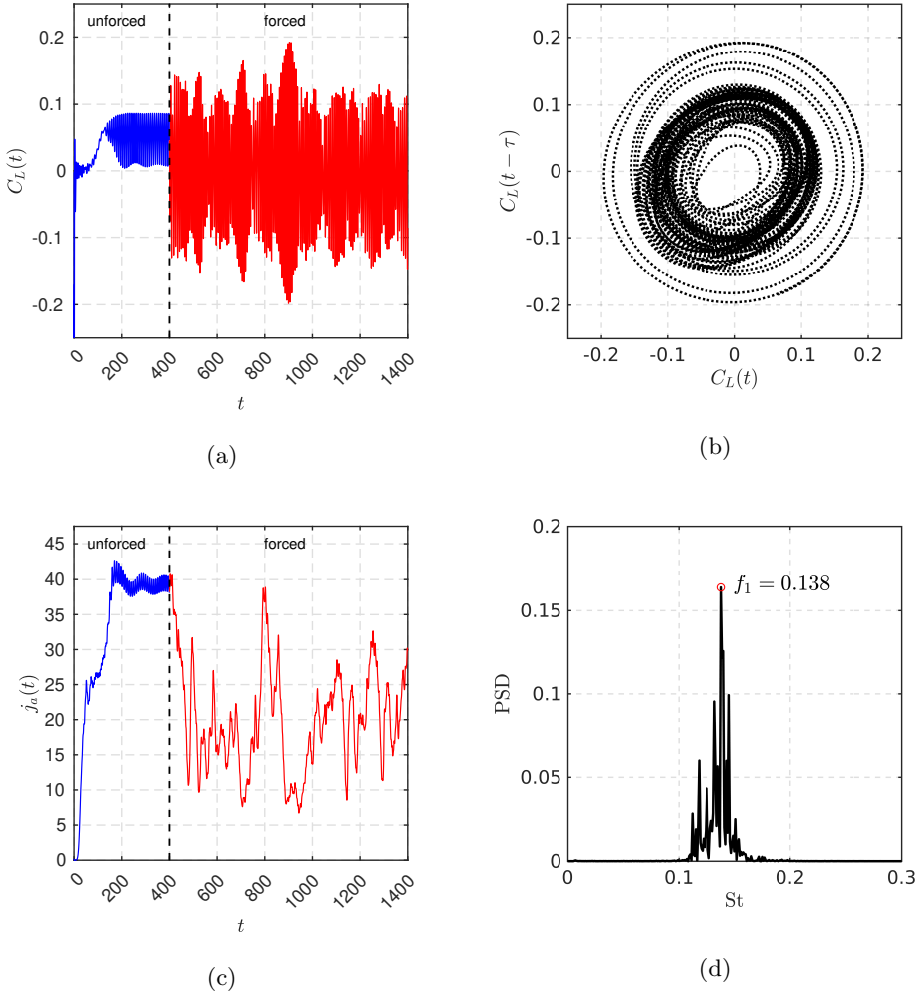


Figure 7: Characteristics of the best base bleeding solution. (a) Time evolution of the lift coefficient C_L , (b) phase portrait (c) time evolution of instantaneous cost function j_a and (d) Power Spectral Density (PSD) showing a broad spectral peak at $f_1 = 0.138$. The control starts at $t = 400$. The unforced phase is depicted in blue and the forced one in red. The phase portrait is computed over $t \in [900, 1400]$ and the PSD is computed on the forced regime $t \in [400, 1400]$.

in the same neighborhood near the initial individuals, crawling along the local gradient to find the minimum.

Figure 10 shows the progression of the best control laws throughout the evaluations after 25 iterations of the exploration/exploitation process. The progression is plotted according to the number of cost function evaluations counted with the dummy index i . Figure 10a depicts the progression of the best control law after each downhill simplex step. We notice that a plateau is reached after 50 evaluations and there are only small variations afterwards. The final control law after 100 evaluations reads

$$[b_1^{\text{EGM}}, b_2^{\text{EGM}}, b_3^{\text{EGM}}]^T = [1.11207, -0.20025, -0.15588]^T \quad \text{with} \quad J_a = 10.85 \quad (4.1)$$

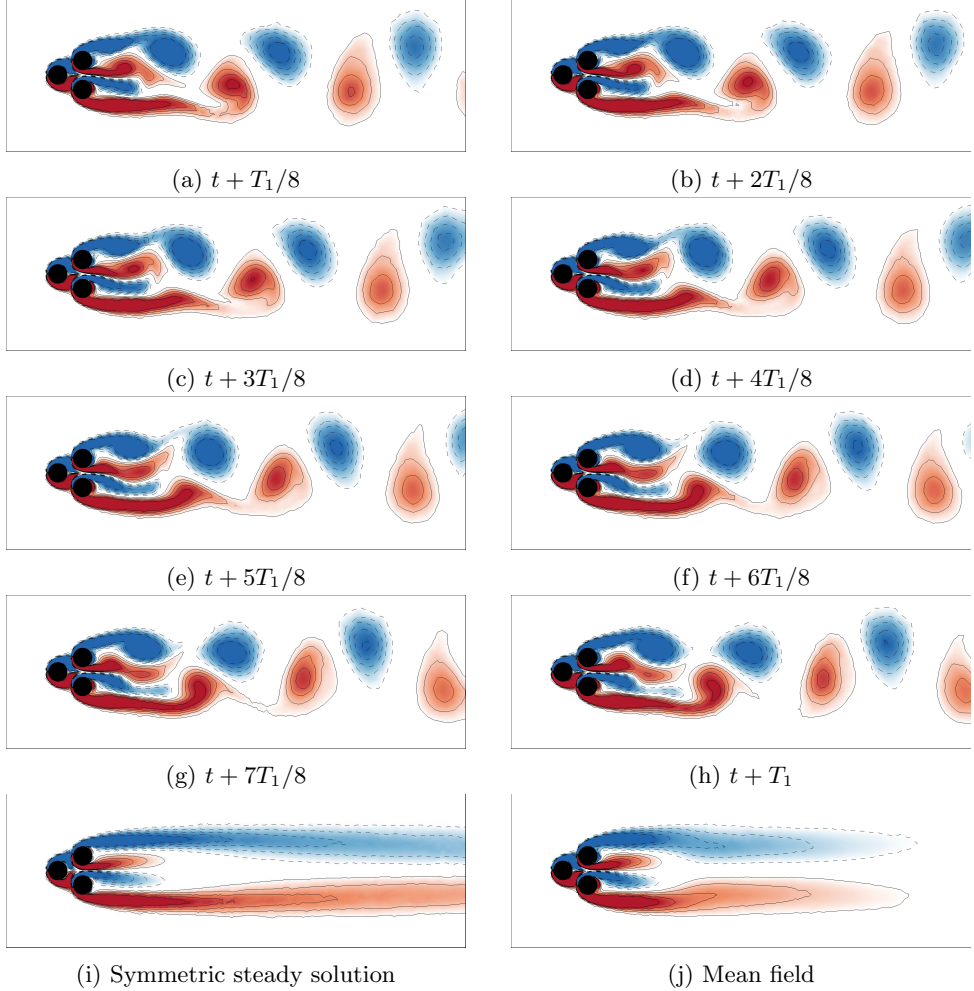


Figure 8: Vorticity fields of the best base bleeding solution. (a)-(f) Time evolution of the vorticity field throughout the last period of the 1400 convective time units, (i) the objective symmetric steady solution and (j) the mean field of the forced flow. The color code is the same as figure 1. T_1 is the period associated to the main frequency f_1 of the forced flow. The mean field has been computed by averaging 100 periods.

From visualizations of the control landscape of J_a in figure 9, we can safely infer that (4.1) describes the global minimum of our search space. Figure 10b shows convergence after 70 evaluations. Thereafter, the downhill simplex iterations show negligible improvements. In the whole EGM optimization, the exploration appears to be ineffective as the initial individuals are close to the minimum. An EGM run with different initial individuals ($[1, 0, 0]^\top$, $[1.5, 0, 0]^\top$, $[1, 1, 0]^\top$ and $[1, 0, 1]^\top$, corresponding to a 25% of the box size shift) have been tested. After a few iterations, this new run started sliding down towards same minimum. This can be explained by the fact that the neighborhood around the minimum is smooth enough for a downhill slide of the exploitation individuals.

The control law (4.1) shows that the front cylinder rotates almost five times faster than the two other cylinders and in opposite direction. The asymmetry in the control law corresponds to the asymmetry in the lift coefficient in figure 11a, where the mean

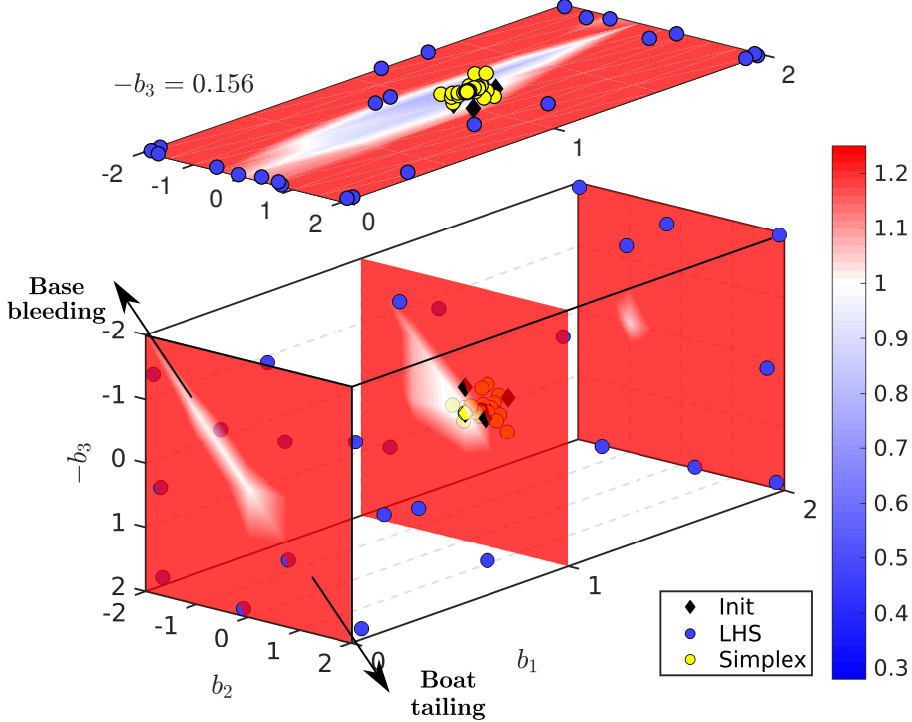


Figure 9: Contour map of J_a/J_0 at the optimal plane $b_3 = b_3^{\text{EGM}} = -0.156$ found with EGM (top) and at different levels of b_1 : $b_1 = 0$, $b_1 = 1$, $b_1 = 2$ (bottom). The colormap denotes white for $J_a/J_0 = 1$, blue for better performances and red for worse performances. The planes are shown with 75% transparency. The four initial conditions $[1, 0, 0]^\top$, $[1.2, 0, 0]^\top$, $[1, 0.4, 0]^\top$ and $[0, 0, 0.4]^\top$ are represented by black diamonds. Blue dots are the control laws build with the exploration phases and yellow dots are the individuals build with the exploitation phases. All the individuals have been projected on the plane $b_3 = -0.156$. The arrows, on plane $b_1 = 0$, depict the base bleeding/boat tailing diagonal studied in section § 4.1. A parametric study shows that the minimum is close to $[b_1, b_2, b_3]^\top = [1, 0, 0]^\top$. The associated cost is $J_a/J_0 = 0.93$.

value is close to -0.7. The flow asymmetry can be visualized in the mean field (figure 12j). The vorticity in the vicinity of the cylinder is directly related to the actuation; thus the upward deflection near the front cylinder is explained by its fast rotation, around 1.1 times the incoming velocity. In addition, the tip of the positive vorticity lobe in the jet is slightly deflected downwards. Figure 12a-8h show that EGM control (4.1) enables a jet fluctuation around vanishing mean, like the best base bleeding solution. Moreover, the phase portrait and the PSD in figure 11 reveal that the flow is purely harmonic. The main frequency $f_2 = 0.140$ is close to the main frequency $f_1 = 0.138$ of the base bleeding solution. Contrary to the best base bleeding solution, the instantaneous cost function j_a stays at low levels with a mean value around 9. The associated normalized cost is $J_a/J_0 = 0.28$. It is worth noting that, even though the control law $[b_1, b_2, b_3]^\top = [1, 0, 0]^\top$ is close to the best one found with EGM, its cost, $J_a/J_0 = 0.93$, is much higher. Moreover, the coarse description of the optimal plane $b_3 = b_3^{\text{EGM}} = -0.15588$, in figure 9 (top), does not show any minimum a priori. This reveals large gradients in the control landscape,

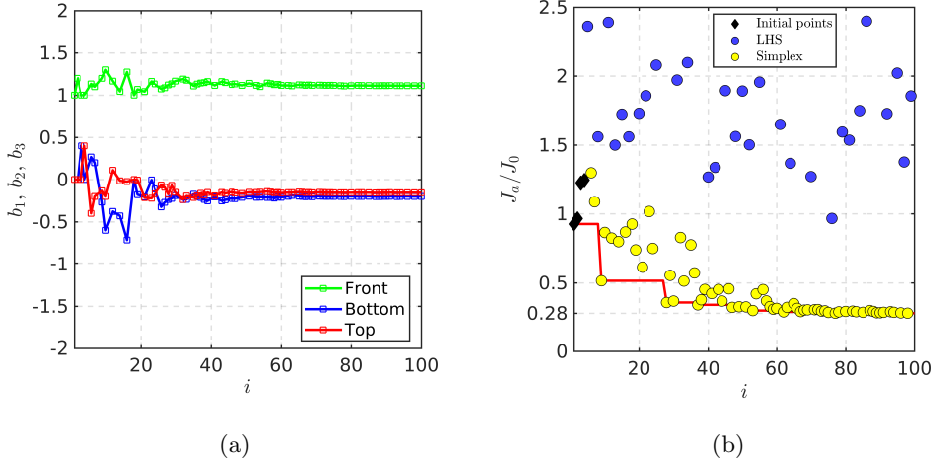


Figure 10: Evolution of b_1 , b_2 and b_3 (left) for each new simplex step indicated by the scattered squares and J_a/J_0 (right) according to the number of evaluations i for the EGM optimization process. The red line on (b) shows the evolution of the best cost. The color code of the dots on (b) is the same as figure 9. The best control law is $[b_1^{\text{EGM}}, b_2^{\text{EGM}}, b_3^{\text{EGM}}]^T = [1.11207, -0.20025, -0.15588]^T$ with $J_a/J_0 = 0.28$.

near the EGM solution, where a small change in the control amplitude can drastically change the associated cost J_a/J_0 .

In addition to the less deflected jet, we notice in figure 12 that vortex shedding differs from the previous solution leading to more symmetric flow. There are now two vortex sheddings of the shear layers one on the upper side and one on the lower side of the flow. These shear layer dynamics hardly interact in the whole domain. Indeed, we notice that the distance between two consecutive vortices increases significantly only before leaving the computational domain which goes along with a slightly upward deflection of the wake. This results in extended vorticity branches in the mean field (figure 12j) but with a lower vorticity level compared to the symmetric steady solution.

As expected, exploring a richer search space improved the stabilization of the flow. However, surprisingly, an asymmetric forcing managed to bring partial symmetry to the flow and reduces the cost function even further compared to the best base bleeding solution. Experimentally, the optimization of the steady fluid pinball actuation also lead to asymmetric forcing Raibaudo *et al.* (2019). The explorative gradient method managed to converge to the global minimum in less than 100 evaluations. The exploration phases had a lesser impact during the optimization process as we initiated the algorithm close to the global minimum. We can expect the exploration phases to play a major role for more complex search space, comprising several minima.

4.3. Feedback control optimization—Gradient-enriched machine learning control

In this section, we optimize a feedback control law again to stabilize the unforced symmetric steady solution. The feedback is provided by 9 velocity signals in the wake as discussed in § 2.3. Several function optimizers can be used to solve the regression problem of equation 2.6. However, a comparison between classical MLC (Duriez *et al.* 2016) and gMLC has been carried out, showing that gradient-enriched MLC not only

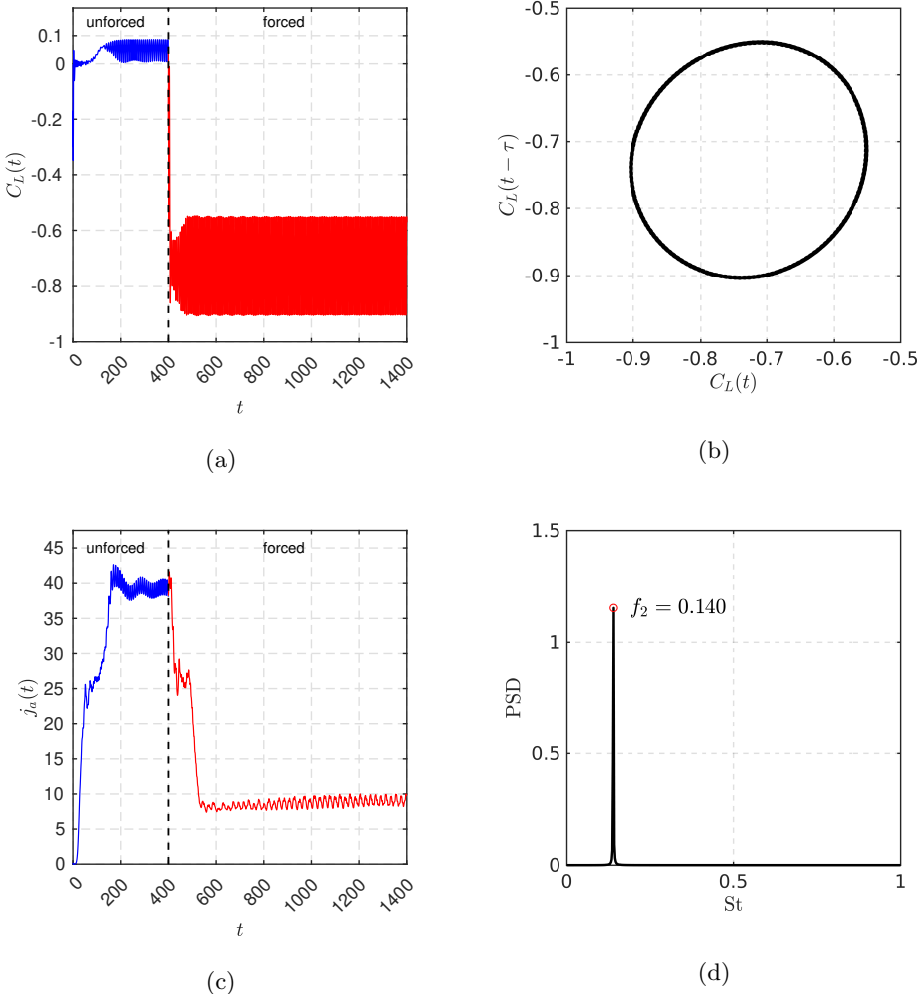


Figure 11: Characteristics of the best steady actuation found by EGM. (a) Time evolution of the lift coefficient C_L , (b) phase portrait (c) time evolution of instantaneous cost function j_a and (d) Power Spectral Density (PSD) showing the only frequency $f_2 = 0.140$ of the forced flow. The control starts at $t = 400$. The unforced phase is depicted in blue and the forced one in red. The phase portrait and the PSD are computed over $t \in [900, 1400]$ the post-transient regime.

converges faster than MLC but also towards a better solution. The comparison between MLC and gMLC is detailed in appendix A.

In the case of the fluidic pinball, the three cylinders are our three controllers thus $Y \subset \mathbb{R}^3$. For the control input space X , we choose a grid of nine sensor downstream measuring either x or y velocity component. The coordinates of the sensors are $x = 5, 6.5, 8$ and $y = 1.25, 0, -1.25$. The six exterior sensors are u sensors while v sensors are chosen for the ones on the symmetry line $x = 0$, so that the signals vanish when the symmetric steady solution is reached. The information of sensors is summarized in table 1. Moreover, in order to take into account the convective nature of the flow, we add time-delayed sensors

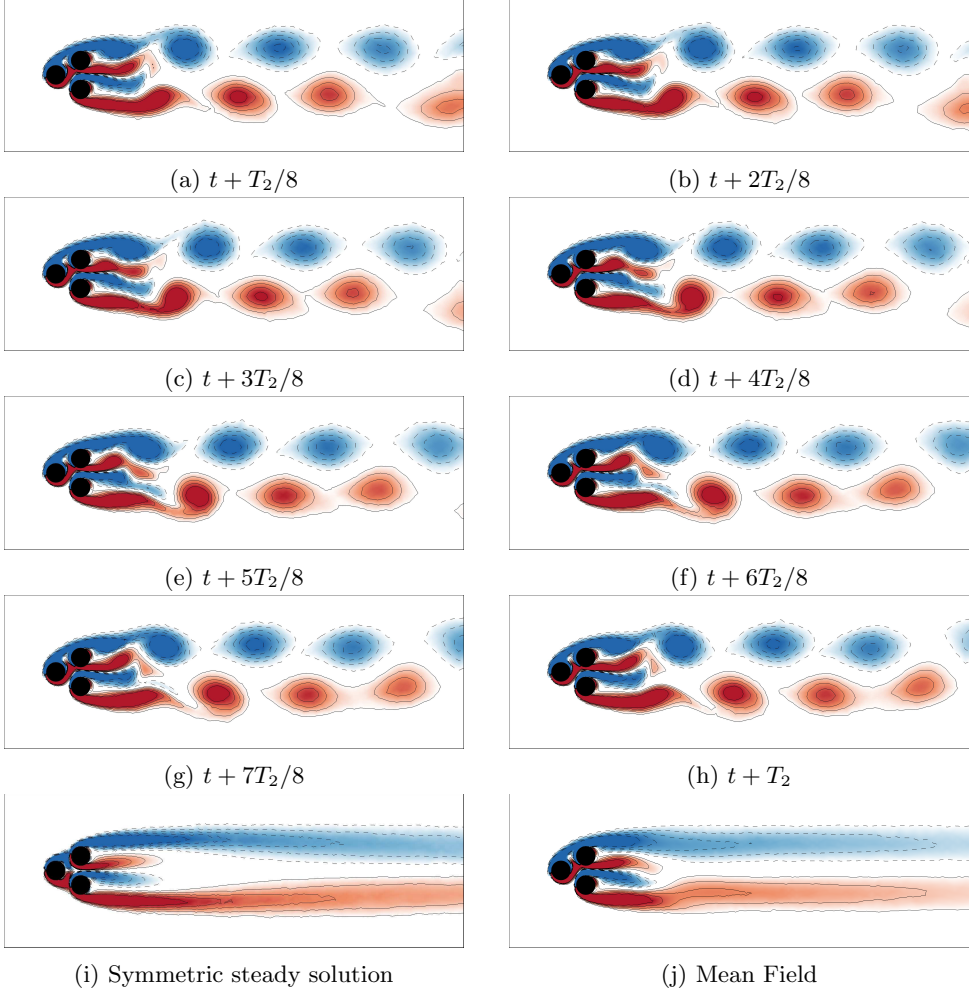


Figure 12: Vorticity fields of the best steady actuation found with EGM. (a)-(f) Time evolution of the vorticity field throughout the last period of the 1400 convective time units, (i) the objective symmetric steady solution and (j) the mean field of the forced flow. The color code is the same as figure 1. T_2 is the period associated to the frequency f_2 of the forced flow. The mean field has computed by averaging over 100 periods.

as inputs of the control laws. The delays are a quarter, half and three-quarters of the unforced natural period, yielding following additional lifted sensor signals:

$$s_{i+9}(t) = s_i(t - T_0/4), \quad s_{i+18}(t) = s_i(t - T_0/2), \quad s_{i+27}(t) = s_i(t - 3T_0/4).$$

Hence, the dimension of the sensor vector s is $9 \times 4 = 36$ and $X \subset \mathbb{R}^{36}$. We do not include time dependent functions in the input space as we aim to stabilize the flow towards the steady solution so an open-loop strategy is not pursued. In appendix B, we detail an open-loop optimization including periodic functions. We show that a symmetric periodic forcing at ≈ 3.5 times the natural frequency, manages to stabilize the flow but at the expense of high actuation power. So periodic functions are not included as inputs in order to avoid costly solution. Thus, $N_b = 3$, $N_s = 36$ and $N_h = 0$. The control laws are then built from 9 basic operations ($+$, $-$, \times , \div , \cos , \sin , \tanh , \exp and \log), 36 sensors

sensor	x -coordinate	y -coordinate	velocity component
s_1	5	1.25	u
s_2	6.5	1.25	u
s_3	8	1.25	u
s_4	5	0	v
s_5	6.5	0	v
s_6	8	0	v
s_7	5	-1.25	u
s_8	6.5	-1.25	u
s_9	8	-1.25	u

Table 1: Summary of sensor information.

signals $s_{i=1..36}$ and 10 constants. The control laws are restricted to the range $[-5, 5]$ to avoid excessive actuation. The basic operations \div and \log are protected in order to be defined on \mathbb{R} in its entirety. The cost function has been computed over 1000 convective time units, so that the post-transient regime is fully established and the transient phase has a lesser weight.

For the implementation of the gMLC algorithm on the fluidic pinball, we start with a Monte Carlo step of $N_{MC} = 100$ individuals, the crossover probability and mutation probability are both set at $P_c = P_m = 0.5$. Indeed, as the evolution phase is mostly an explorative phase, the mutation probability is increased, from 0.3, in previous studies, to 0.5, to improve the exploration capability. Moreover, even though crossover is an exploitative operator, it is likely to find new minima thanks to recombinations of radically different control laws. That is why, the crossover and mutation probabilities are both set to 0.5. The dimension of the subspace is set to $N_{sub} = 10$, so it is large enough to explore a rich subspace but not too large to avoid a slowdown in the optimization process. Evidently with a subspace of higher dimension the control law can be more finely tuned. To assure that the subplex step effectively goes down the local minimum, we choose to evaluate $N_G = 50$ individuals during the exploitation phase. Test runs with $N_G = 5$ have been carried out and showed that the learning process was slower. We believe one reason is that each exploration phase changes systematically the subspace, which makes it difficult for the subplex to improve effectively in only a few steps, thus, subplex has almost no benefit in the early phases. Table 2 summarizes all the parameters for gMLC. The secondary optimization problem (equation 3.1) used to build a matrix representation for the control laws, is solved with LGP. To speed up the computation, we choose to solve the secondary optimization problem with 100 individuals evolving through 10 generations. Finally, our implementation is enhanced by a screening of the individuals to avoid reevaluating individuals that have different mathematical expressions but are numerically equivalent, just as (Cornejo Maceda *et al.* 2019). This screening is used only in steps where the individuals are generated stochastically, meaning in the Monte Carlo step and in the exploration phases. This improvement is also used in LGP to solve the secondary optimization problem.

Figure 13 presents the learning process of gMLC for the stabilization of the fluidic pinball. We notice that the first exploration phase, individuals $i = 101, \dots, 150$, already improved the best cost compared to the Monte Carlo phase. The following exploitation, individuals $i = 151, \dots, 200$, present a steep descent, improving the best solution even further. During this phase, we notice a clear trend for the cost of the new individuals. This

Parameter	value
N_b	3
N_s	9 sensors \times 4 delays = 36 sensor signals
N_h	0
N_{MC}	100
N_{sub}	10
P_c	0.5
P_m	0.5
N_G	50
Operations	$+, -, \times, \div, \cos, \sin, \tanh, \exp, \log$
Number of constants	10
Constant range	[-1,1]

Table 2: gMLC parameters for the fluidic pinball.

trend indicates that the simplex is going down towards a minimum. But this descent is interrupted by the next exploration phase. Individuals $i = 201, \dots, 250$, greatly improve the best solution. Particularly, two individuals have a much lower cost than the ones in the simplex, suggesting that new minima have been found. The next exploitation phase with individuals $i = 251, \dots, 300$ brings no improvement. The high values of cost in the exploitation steps following the exploration phases is explained by the fact that as we are exploring new minima, shrink steps must be performed to bring the simplex towards the new minima; and the shrink steps replaces all individuals in the simplex except the best one. As we are leaving one minimum for another one, the intermediate values can be arbitrarily high until the simplex reached the neighborhood of the new minimum. The next exploration phase with individuals $i = 301, \dots, 350$ also give good individuals that have been included in the simplex. After 350 evaluations, the only improvements are performed by exploitation phases. Even if the best cost keeps decreasing slowly, the improvements are small, indicating that we are close to the minimum. Once we reach a plateau, further improvement can only be performed if an exploration phase finds an individual close to a better minimum. That is why after 800 individuals, we performed only exploration phases. The final control law build with gMLC reads

$$\begin{aligned}
b_1^{\text{gMLC}} &= -0.0004 \sin(\cos(s_{30})) - 0.0034(s_6 + s_{22}) - 0.0033(\log(s_{11})) - 0.0305(s_3) \\
&\quad - 0.0098(s_{16} + s_{15}) + 0.0055s_{35}(s_{16} + 0.31016) - 0.0091(s_3 - s_{23}) \\
&\quad + 0.9206 \tanh(s_{16}) - 0.1238 \cos(s_{31}) + 0.1907, \\
b_2^{\text{gMLC}} &= -0.0459(\log(\log(s_{31}))) - 0.1946, \\
b_3^{\text{gMLC}} &= -0.0004(0.841471s_{34} - s_{36}) - 0.0043 \log(s_9) - 0.0022(s_{25} - s_{16}) \\
&\quad - 0.0098(\cos(s_3) - s_{16}) + 0.9206 \log(\tanh(\exp(s_2))) - 0.0295 \\
J_a &= 7.82.
\end{aligned} \tag{4.2}$$

Figure 14 presents the characteristics of the flow controlled by the best control law \mathbf{K}^{gMLC} built with gMLC. This control law is detailed later specially in table 3. In figure 14a, we can see that even if the resulting lift coefficient is still asymmetric, the mean value (around -0.1) is closer to 0 as compared to the EGM solution. The PSD in figure 14d shows a dominant frequency at $f_3 = 0.144$ and one of its higher harmonics. A small peak can be seen for $f_4 \approx 0.016$. The nonlinear interaction between the frequencies $f_3 = 0.144$ and $f_4 = 0.016$ gives rise to another small peak at $f_5 = 0.160$. The phase portrait in figure 14b reveals drifts in pronounced oscillations due to the low frequency

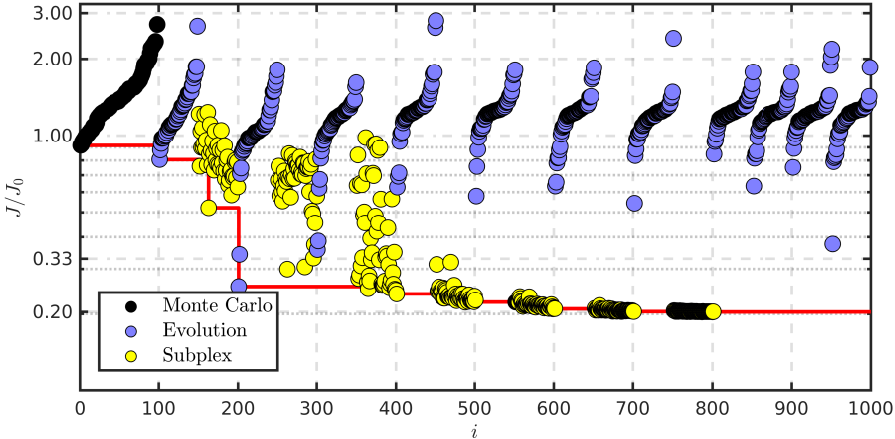


Figure 13: Distribution of the costs during the gMLC optimization process. Each dot represents the cost J_a/J_0 of one individual. The color of the dots represents how the individuals have been generated. Black dots denote the individuals which are randomly generated (Monte Carlo). Blue dots refer to individuals which are generated from a genetic operator (exploration). And yellow dots correspond to individuals arising from the subplex method (exploitation). The individuals from the Monte Carlo step and the exploration phase have been sorted following their costs. The red line shows the evolution of the best cost. The vertical axis is in log scale.

modulation. The presence of the dominant frequency $f_3 = 0.144$ and its harmonic in the spectrum is consistent with the periodic behavior of the flow. The $f_4 = 0.016$ peak is responsible for the width of a predominant limit-cycle dynamics in the phase portrait.

The evolution of the instantaneous cost function j_a in figure 14c shows a plateau after 200 convective time units, reaching an even lower level (around 6), compared to the EGM solution (around 9). The associated cost $J_a/J_0 = 0.20$ is better than the EGM solution at $J_a/J_0 = 0.28$.

Table 3, 4 and figure 15 give more details on the control law \mathbf{K}^{gMLC} built with gMLC. Firstly, we can see that even though the simplex comprises $N_{\text{sub}} = 10$ individuals, subplex build the control law \mathbf{K}^{gMLC} by linearly combining 14 control laws. Indeed after a few iterations of simplex, all the individuals are eventually a linear combination of the initial individuals forming simplex. When a new individual is introduced in the basis thanks to the exploration phase, the exploitation phase will combine the remaining individuals with the new one, making the next individual a linear combination of more than 10 individuals. It is important to note that even after the introduction of new individuals with the exploration phase, the subspace to explore changes but the dimension remains. In this case, with $N_{\text{sub}} = 10$, the dimension of the subspace is 9. The repetition of this process builds each time more complex control laws. Thus, in table 3, individuals $i = 11, 12, 13, 14$ have been introduced thanks to exploration phases. The control laws with the strongest weights are $i = 11, 13$ and 14 , whereas the weight associated with the other control laws are at least one order of magnitude lower. Control law $i = 11$ is also the one with the lowest cost $J_a/J_0 = 0.26$. \mathbf{K}^{gMLC} is then mainly based on $i = 11$ and corrected by the remaining control laws. This indicates that on the last phase of the learning, it is the minimum in the neighborhood of $i = 11$ that has been found.

Moreover, table 3 shows that all three control components $b_1^{\text{gMLC}}, b_2^{\text{gMLC}}$ and b_3^{gMLC}

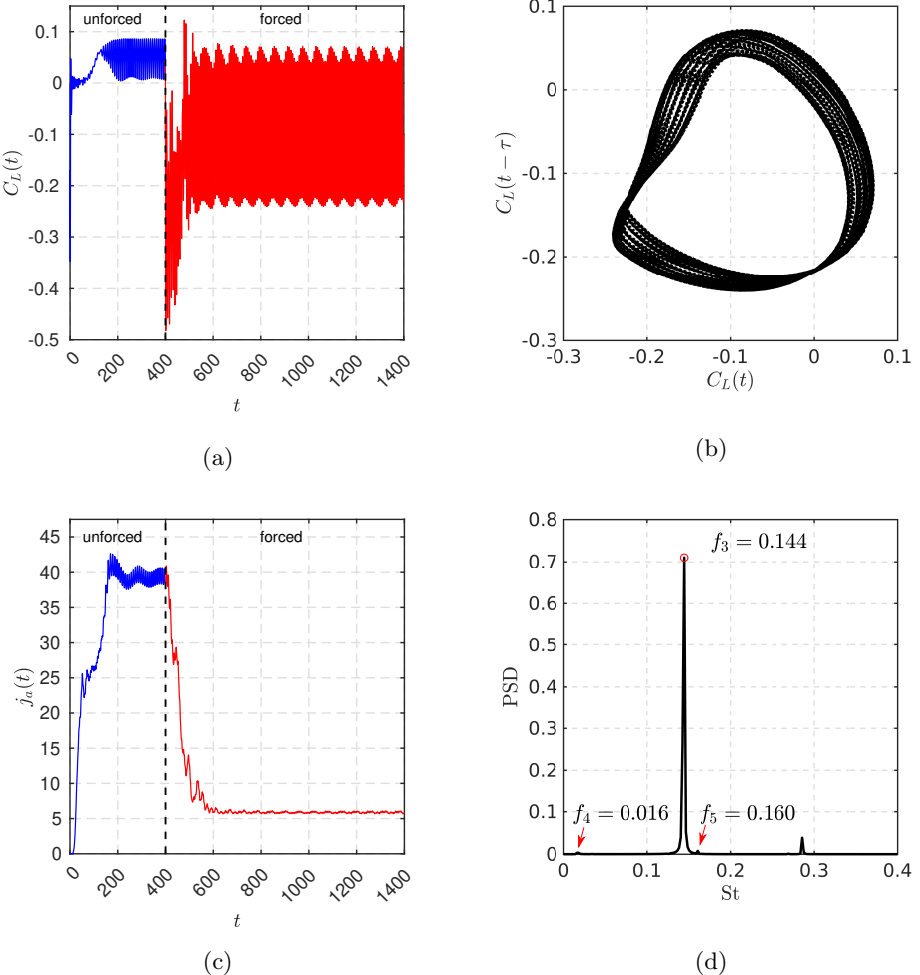


Figure 14: Characteristics of the flow controlled by the best feedback control law found with gMLC. (a) Time evolution of the lift coefficient C_L , (b) phase portrait, (c) time evolution of instantaneous cost function j_a and (d) Power Spectral Density (PSD) showing the frequency $f_3 = 0.144$ of the forced flow, one of its harmonics and two low-power frequencies $f_4 = 0.016$ and $f_5 = 0.160$. The control starts at $t = 400$. The unforced phase is depicted in blue and the forced one in red. The phase portrait and the PSD are computed over $t \in [900, 1400]$, during the post-transient regime.

of the gMLC control law include sensor information. However, figure 15 shows that the actuation command associated with \mathbf{K}^{gMLC} for the two rearward cylinders (b_2 and b_3) are nearly constant. This is partially due to the low weights associated to the control laws with sensor signals. We can also assume that the sensor signals cancel each other, leading to such low peak-to-peak amplitudes. Table 4 shows the characteristics of the actuation command during the post-transient regime. A spectral analysis shows that the main frequency of the actuation command for the front and bottom cylinder are twice the main frequency of the flow f_3 , revealing that the actuation is a function of the flow. Thus, gMLC managed to build a combination between asymmetric steady forcing and

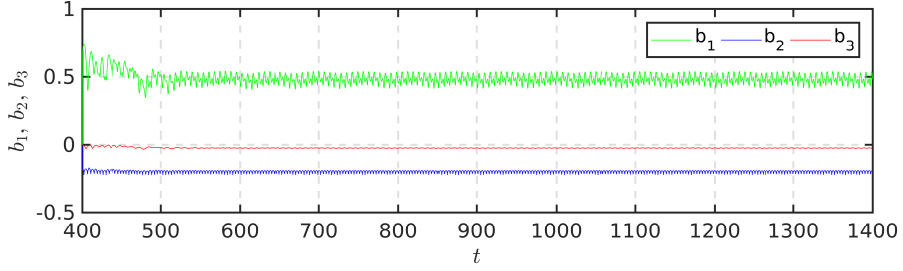


Figure 15: Time series of the actuation command for the best feedback control law found with gMLC.

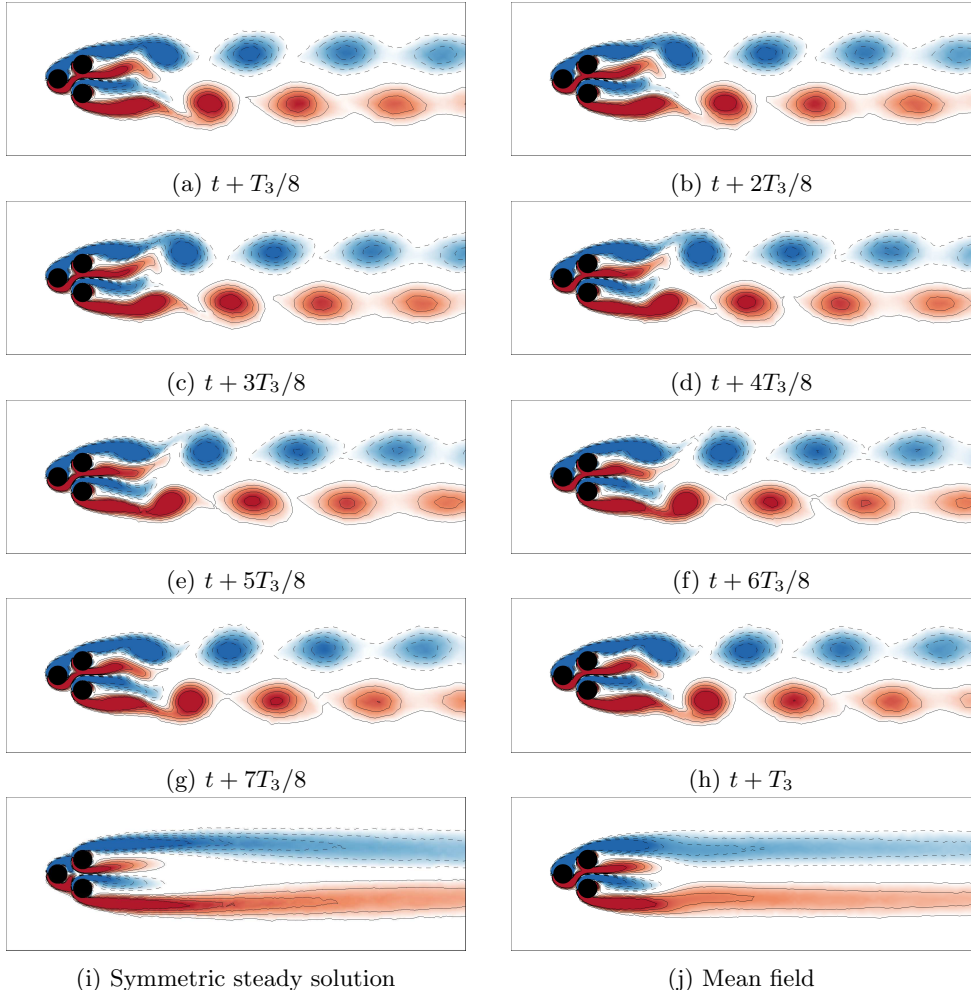


Figure 16: Vorticity fields of the best feedback control found with gMLC. (a)-(f) Time evolution of the vorticity field throughout the last period of the 1400 convective time units, (i) the objective symmetric steady solution and (j) the mean field of the forced flow. The color code is the same as figure 1. T_3 is the period associated to the frequency f_3 . The mean field has been computed by averaging 100 periods.

#	b_1	b_2	b_3	weight	J_a / J_0
1	$\sin(\cos(s_{30}))$	0	$0.841471s_{34} - s_{36}$	-4×10^{-4}	0.91
2	$s_6 + s_{22}$	0	0	-3.4×10^{-3}	0.94
3	0	0	$\log(s_9)$	-4.3×10^{-3}	0.97
4	0	0	$s_{25} - s_{16}$	-2.2×10^{-3}	0.97
5	$\log(s_{11})$	0	0	-3.3×10^{-3}	0.95
6	s_3	0	0	-3.05×10^{-2}	0.92
7	$s_{16} + s_{15}$	0	$\cos(s_3) - s_{16}$	-9.8×10^{-3}	0.97
8	$s_{35}(s_{16} + 0.31016)$	0	0	5.5×10^{-3}	0.80
9	$s_3 - s_{23}$	0	0	-9.1×10^{-3}	0.88
10	1	$\log(\log(s_{31}))$	0	-4.59×10^{-2}	0.93
11	tanh(s₁₆)	-0.187071	log(tanh(exp(s₂)))	9.206 × 10⁻¹	0.26
12	0.540302	-0.144304	-0.0144074	6.87×10^{-2}	0.34
13	cos(s₃₁)	-0.144304	-0.0144074	-1.238 × 10⁻¹	0.36
14	0.949948	-0.144304	-0.0144074	2.100 × 10⁻¹	0.39

Table 3: Summary of the 14 control laws composing K^{gMLC} described in equation (4.2). For each control law, we present b_1 , b_2 , b_3 , the associated weight and the reduced cost J_a/J_0 . The three best control laws are #11, #13 and #14.

cylinder	mean value	main frequency	peak-to-peak amplitude
front (b_1 , green)	0.48	$2f_3$	0.12
bottom (b_2 , blue)	-0.19	$2f_3$	0.03
top (b_3 , red)	-0.02	f_3	< 0.01

Table 4: Summary of control law information. The frequencies and peak-to-peak amplitude have been computed on the post-transient regime.

feedback control. Finally, like EGM, the best solution found is asymmetric but with lower amplitudes. Consequently, the associated actuation power is lower compared to general steady actuation found with EGM: $J_b = 0.12$ for the general steady actuation and $J_b = 0.03$ for the feedback control law found with gMLC.

The controlled flow is depicted over one period in figure 16a-16h. First, we notice that the jet fluctuates around a vanishing mean, as for the EGM actuation. Also, the vortex sheeding of the upper and lower shear layers hardly interact. Compared to the EGM solution, the stability of the wake is improved as the two Kelvin-Helmholtz vortices keep their transverse distance to the symmetry line until the very end of the computational domain. This is explained by the re-energization of the shear layers thanks to the vigorous rotation of the front cylinder at twice the main frequency f_3 of the controlled flow, like Protas (2004). The mean field, in figure 16j, is similar to the symmetric steady solution. Indeed, we notice that the vorticity regions extend to the end of the computation domain, like the symmetric steady solution. Like for the best general steady actuation, the region near the cylinders is non-symmetrical due to the action. However, contrary to the symmetric steady solution, the mean field of the feedback control has a narrower region between the vorticity regions upstream and a wider region downstream.

As expected, gMLC manages to found a new solution that surpasses the best general

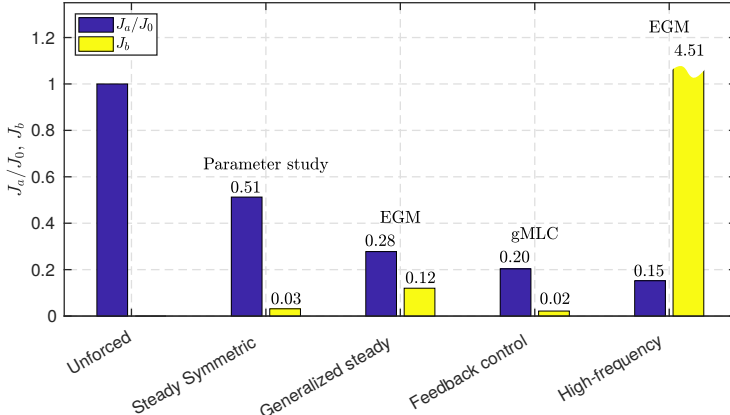


Figure 17: Summary of the performances for the best solutions for each method/search space couple. The relative distance to the symmetric steady solution J_a/J_0 and the actuation power J_b is represented. The costs are computed over 1000 convective time units. The last column shows the results for a periodic forcing optimization performed with EGM, see appendix B.

steady actuation found with EGM. Surprisingly, gMLC built a non-trivial solution, combining asymmetric steady forcing and feedback control for the front cylinder. Interestingly, gMLC composed a control law that forces the flow at twice the main frequency. In addition, compared to the best general steady actuation, the actuation power is significantly reduced. Lastly, the learning process of gMLC exploited both the evolution phases and the simplex steps to rapidly build better solutions. Thanks to the evolution phases, new minima have been successfully found and thanks to the simplex steps, the solutions have been improved even more. The progress of the subplex steps show that local gradient information can be exploited in a subspace of an infinite dimension space to minimize a cost function. Building on this success, we believe that gradient-enriched MLC will greatly accelerate the optimization of control laws for MIMO control as compared to the linear genetic programming control.

5. Conclusions

We have stabilized the wake behind a fluidic pinball with three independent cylinder rotations in successively larger search spaces for control laws. Figure 17 summarizes the corresponding performances quantified by the average distance between the controlled flow and the steady symmetric solution. First, steady symmetric forcing is employed. A base bleed with a cylinder rotation of 28% of the oncoming velocity leads to a flow which is 49% closer to the symmetric solution than the unforced attractor. Other studies also report about a stabilizing effect of base bleed on bluff body wakes (Wood 1964; Bearman 1967). In contrast, Coanda forcing, i.e., two symmetric cylinder rotations which accelerate the outer flow, may completely stabilize the flow. Yet, this new wake has no long vortex bubble and is further away from the symmetric steady solution than the unforced vortex shedding.

Second, a general non-symmetric actuation is optimized with the explorative gradient method. Surprisingly, an asymmetric actuation reduces the average distance between the flow and the steady target solution further to 28% of the unforced value. This asymmetric

actuation leads to shear layer vortices which do not interact and thus do not form von Kármán vortices. The mean flow is slightly asymmetric, but largely mimics the elongated steady symmetric solution. The price for the better performance is a larger actuation power (see figure 17). Intriguingly, machine learning control also leads to distinctly asymmetric actuation in experiments (Raibaudo *et al.* 2019) and simulations (Cornejo Maceda *et al.* 2019) for other cost functions.

Third, a feedback actuation obtained from gradient-enriched machine learning control brings the flow even closer to the steady target solution. The associated actuation power is smaller than the previous optimized steady actuations (see figure 17). The actuation is a combination of asymmetric steady forcing and phasor control. The resulting flow looks similar to the optimal asymmetric steady forcing.

The feedback control does not seem to have the authority to completely stabilize the symmetric target solution, like for the cylinder wake controlled by a volume force (Gerhard *et al.* 2003). The wake can be ‘almost’ stabilized for short periods of time, starting from the unforced flow. Then, new coherent structures emerge and lead to residual shear-layer shedding. This lack of complete authority for stabilization may be explained by the complexity of the dynamics. The fluidic pinball has a primary instability associated with von Kármán vortex shedding, a secondary pitchfork instability associated with the centerline jet, and two Kelvin-Helmholtz instabilities of the top and bottom shear layer.

Intriguingly, symmetric high-frequency forcing can bring the flow even closer to the steady target solution but with an actuation power which is roughly two orders of magnitude larger than the previous control laws (see figure 17). Protas (2004) and Thiria *et al.* (2006) also find a stabilizing effect of high-frequency forcing on vortex shedding. The thickening of the shear layers by high-frequency vortices reduces the gradients and thus the instability. To summarize, machine learning control has automatically discovered well known stabilizing mechanisms, like base bleed and phasor control, but added an unexpected asymmetric forcing and combination of this open-loop actuation and phasor feedback for improved performance.

The presented stabilizations are expected to be independent of the employed optimizer as different approaches lead to very similar results. The chosen optimizers balance exploitation (downhill descend of found minima) and exploration (search for better minima). The optimization has been effected in a three-dimensional parameter space for steady forcing and a feedback space with three actuation inputs and nine sensing outputs. Starting point is Latin hypercube sampling as exhaustive exploration of the parameter space and linear genetic programming control as effective regression solver with explorative and exploitative features. The search has been significantly accelerated by intermittently adding gradient-based descends. The resulting explorative gradient method and gradient-enriched machine learning control seem efficient for both exploration and exploitation. Future research shall focus on accelerated learning.

The control performance may be further improved by allowing for more general control laws comprising the history of the sensor signals, like in ARMAX-based control (Hervé *et al.* 2012). Other generalizations of machine learning control include multiple pre-defined operating conditions, adaptive control for unknown operating conditions, automated learning of the response model from the control law to performance following Fernex *et al.* (2020) and automated learning of control-oriented modeling based on Li *et al.* (2020a). The fluidic pinball represents an attractive plant of sufficient dynamic complexity with manageable computational load for these developments.

Acknowledgements

The authors thank Nan Deng and Luc Pastur for the fruitful discussions and enlightening comments. This work is supported by the French National Research Agency (ANR) via FLOWCON project “Contrôle d’écoulements turbulents en boucle fermée par apprentissage automatique” funded by the ANR-17-ASTR-0022, the German National Science Foundation (DFG grants SE 2504/1-1 and SE 2504/3-1), the iCODE Institute, research project of the IDEX Paris-Saclay and by the Hadamard Mathematics LabEx (LMH) through the grant number ANR-11-LABX-0056-LMH in the “Programme des Investissements d’Avenir”.

Declaration of interests

The authors report no conflict of interest.

Appendix A. Comparison between MLC and gMLC

In this appendix, we compare the performances of a machine learning control (MLC), based on linear genetic programming control (Li *et al.* 2018; Zhou *et al.* 2020), and the proposed gradient-enriched MLC (gMLC) variant for the stabilization of the fluidic pinball. gMLC is described in section § 4.3. MLC differs from gMLC in two respects. First, the evolution is from generation to generation, i.e., groups of individuals. Second, unlike gMLC, no gradient information is employed. The first generation of randomly generated individuals evolves through generations thanks to three genetic operations:

- *Crossover*: a stochastic recombination of two individuals, giving two new individuals exploiting parts of the first two individuals;
- *Mutation*: a stochastic change in one individual, giving one new individual more or less different from the previous one;
- *Replication*: an identical copy of one individual, assuring memory of good individuals throughout the generations.

During the evolution process, the better-performing individuals are selected with larger probability to build new individuals thanks to the genetic operators. The best individuals are selected thanks to a tournament selection method. As in Duriez *et al.* (2016), we choose a tournament selection of size 7 for 100 individuals. A genetic operation is chosen randomly following given probabilities: the crossover probability P_c , the mutation probability P_m and the replication probability P_r . The probabilities add up to unity $P_c + P_m + P_r = 1$. The set of parameters $[P_c, P_m, P_r]^\top = [0.6, 0.3, 0.1]^\top$ suggested in Duriez *et al.* (2016) have been chosen for MLC. A parametric study varying P_c , P_m and P_r with a 0.1 step has been carried out on the stabilization of a Landau oscillator by forcing only on one of its components. As MLC is a stochastic process, we perform 100 test runs for each probability combination. This parametric study reveals that this probability combination $[P_c, P_m, P_r]^\top = [0.6, 0.3, 0.1]^\top$ is one the best. Among all the probability combinations, this combination is one of those that converges towards better solutions in average, with one of the lowest dispersion of the final solutions over the 100 test runs, showing that this combination is also one of the more robust. This or a very similar probability combination has already been used in Duriez *et al.* (2016) and dozens of experiments (Noack 2019).

In addition to *crossover*, *mutation* and *replication*, we transfer the best individual of the previous generation to the next one via the *elitism* operation. This operation assures that the best individual is always in the latest generation so that ‘the winner does not get lost’.

The architecture of the linear programming control laws are the same for MLC and gMLC, including the mathematical operations, number of constants, number of registers, as well as inputs and outputs (see table 2).

The cost function is evaluated over 1000 convective time units, both in MLC and gMLC.

The MLC and gMLC algorithms are compared over 1000 evaluations. For MLC, a population of 100 individuals is chosen to evolve over 10 generations. For a fair comparison, MLC and gMLC share the same initial Monte Carlo generation, comprising the first 100 randomly generated individuals. Figure 18 shows the distribution of the costs J_a/J_0 as a function of the evaluations. We notice that for both algorithms the first exploration phase makes great improvement. In the second generation, the best cost is 0.80 for gMLC and 0.70 for MLC. Note that MLC's better performance can be expected as the 101th individual is the best of the whole generation, i.e., MLC has tested two times more individuals than gMLC. After testing 200 individuals, gMLC surpasses MLC thanks to the subplex steps, reaching a cost $J_a/J_0 = 0.52$. For the second evolution phase, both MLC and gMLC perform well reaching low levels of J_a/J_0 : 0.36 for MLC and 0.26 for gMLC. Then MLC achieves only small progress after 900 evaluations, the cost improves from 0.36 to 0.33. The series of blue dots at $J = 0.36$ from $i = 201$ to $i = 900$ represents several instances of the best individual of generation 3, duplicated thanks to elitism. For gMLC, figure 13 shows that evolution phases do not bring any progress after 250 evaluations and further improvement is made thanks to the subplex steps. As described in section § 4.3, the evolution phases help to enrich the simplex subspace. The subplex steps manage to reduce the cost function from 0.26 to 0.20. We notice that after 600 evaluations all new subplex individuals have the same cost. Hence, gMLC surpasses MLC with a smaller number of evaluations and enables improvement/fine tuning of the control laws in the final phase.

Appendix B. Optimal periodic forcing

In this appendix we aim to stabilize the symmetric steady solution thanks to a symmetric periodic forcing. In this case, the two back cylinders oscillating in opposite directions whereas the front cylinder stays still. The control ansatz is the following:

$$\begin{aligned} b_1 &= 0 \\ b_2 &= B \cos(2\pi F t) \\ b_3 &= -B \cos(2\pi F t) \end{aligned}$$

with B , the amplitude of the oscillations, and F , the frequency, being the two parameter to optimize. The search space is limited to $[B, F/f_0]^\top \in [0, 5] \times [0, 10]$ as higher amplitudes and frequencies would be beyond our solver capabilities. This two-dimensional search space is explored with EGM. The contour plot in figure 19 depicts the search space based on J_a/J_0 and J_b . The contour plot has been produced thanks to simulations for $B \in \{0.1, 0.5, 1, 2, 3.5, 5\}$ and $F/f_0 \in \{0.1, 0.5, 1, 2, 3.5, 5, 7.5, 10\}$. The steps are finer for low frequencies and low amplitudes. The individuals have been evaluated over 250 convective time units. We notice that there is only one minimum on the plane, close to $[B, F/f_0]^\top = [3.51, 3.19]^\top$. Also, forcing at frequencies close to the natural frequency resonates with the flow and increases drastically the distance to the steady solution for high amplitudes. For J_b , the contour map expectedly displays high values at high frequencies and large amplitudes. The three initial control laws for EGM are the center of the box and increments of 1/5 of the box in each direction: $[2.5, 5]^\top$, $[3, 5]^\top$, $[2.5, 6]^\top$.

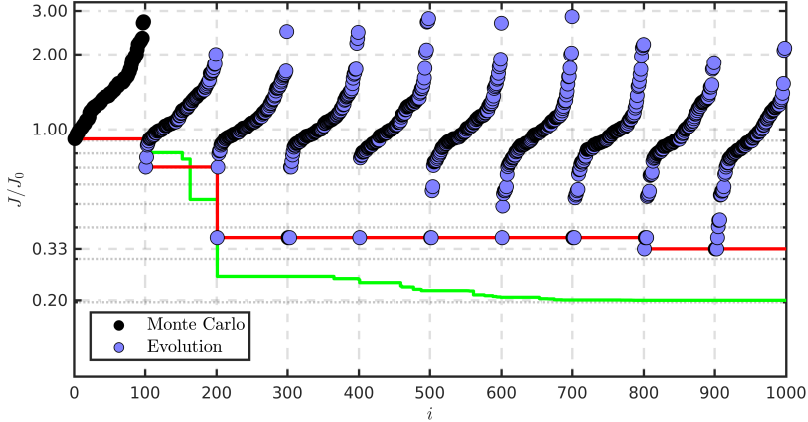


Figure 18: Distribution of the costs during the MLC optimization process. Each dot represents the cost J_a/J_0 of one individual. The color of the dots represent how the individuals have been generated. Black dots for the individuals randomly generated by a Monte Carlo process (individuals $i = 1, \dots, 100$), blue dots for the individuals generated from a genetic operator (individuals $i = 101, \dots, 1000$). For each generation the individuals have been sorted according to their cost. The red line shows the evolution of the best cost for the MLC optimization process. The green curve corresponds to the gMLC optimization process. The vertical axis is in log scale.

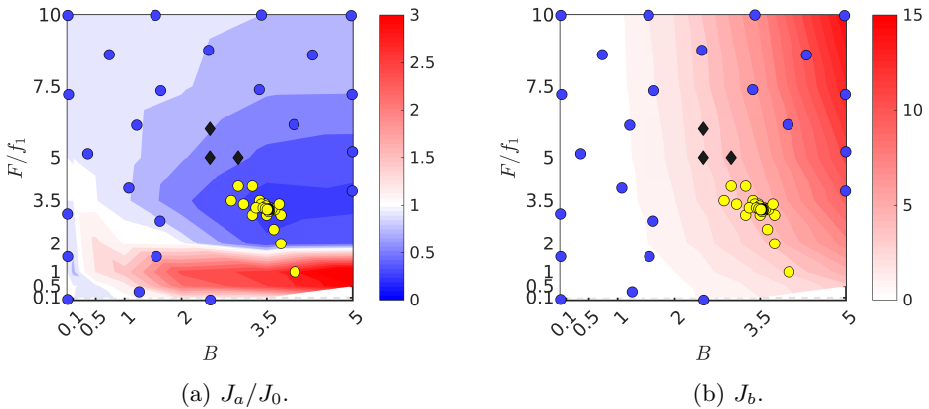


Figure 19: Contour plot for J_a/J_0 (a) and J_b (b) as a function of the amplitude B and the normalized frequency F/f_0 . For (a), blue (red) regions denote good (bad) performances while white regions correspond to costs that are equivalent to the natural flow. For (b), the color code describes the actuation energy. The symbols represent the individuals tested with EGM: black diamonds for the initial conditions, blue solid circles for exploration phases and yellow solid circles for the exploitation phases. For the legend, refer to figure 9.

As expected, the LHS steps (in blue) spread rather evenly in the domain whereas the simplex steps (in yellow) quickly descend into the global minimum.

Figure 20 shows the progression of the best individual throughout the evaluations. The EGM optimization process converges after few tests as J_a/J_0 , the amplitude and the

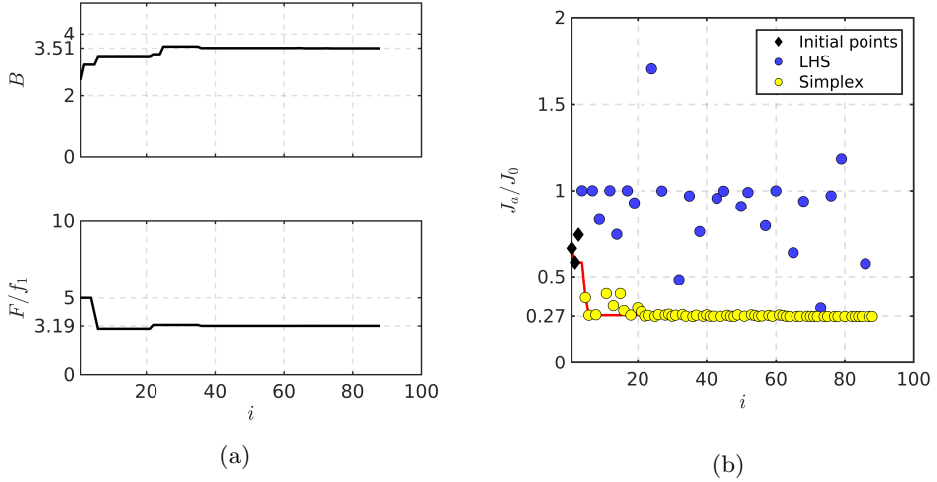


Figure 20: Evolution of (a) the amplitude B and the normalized frequency F/f_0 and (b) the reduced cost J_a/J_0 as a function of the number of evaluations i , for the EGM optimization process. The red line in (b) shows the evolution of the best cost. The evaluation time is 250 convective time units.

frequency reach asymptotic values, without any significant improvement afterwards. The parameters of the best symmetric periodic forcing are denoted by the superscript ‘EGM’ and read

$$\begin{aligned} B^{\text{EGM}} &= 3.51, \\ F^{\text{EGM}}/f_0 &= 3.19. \end{aligned}$$

The proximity between the initial values and the aimed minimum certainly accelerates the observed convergences. Figure 21 show the evolution of the lift coefficient, the phase portrait, the power spectral density and the instantaneous cost function j_a for the controlled flow. The lift coefficient presents rather symmetric low amplitude oscillations, see figure 21a. This goes along with the flow symmetry in figure 22a-22h. The oscillations are explained by the remaining vortex shedding on both the upper and lower side of the fluidic pinball. Even though the far field is close to the symmetric steady solution, this periodic solution changes radically the near field profile. The jet is completely flattened. We can identify parts of the two vorticity branches close to the cylinders in figure 22c, 22d and 22e. Moreover, the vorticity around the cylinders is more intense compared to the initial steady solution. This difference is present in the final mean value j_a in figure 21c and is responsible for the high actuation power expense, $J_b = 4.51$. The phase portrait shows a periodic regime, though deformed by the harmonics. The mean frequency $f_6 = 0.398$ is slightly lower than the forcing frequency $F^{\text{EGM}} = 0.37$ and much lower than the natural frequency, showing that it is not just a simple frequency locking, but a nonlinear frequency crosstalk. The non centered phase portrait indicates that there is still an asymmetry in the flow, that may be a residual effect of the grid’s asymmetry. The mean field in figure 22j is similar to the symmetric steady solution, however the jet completely vanished, in addition, the distance between the upper and lower vorticity branches is wider compared to the symmetric steady solution.

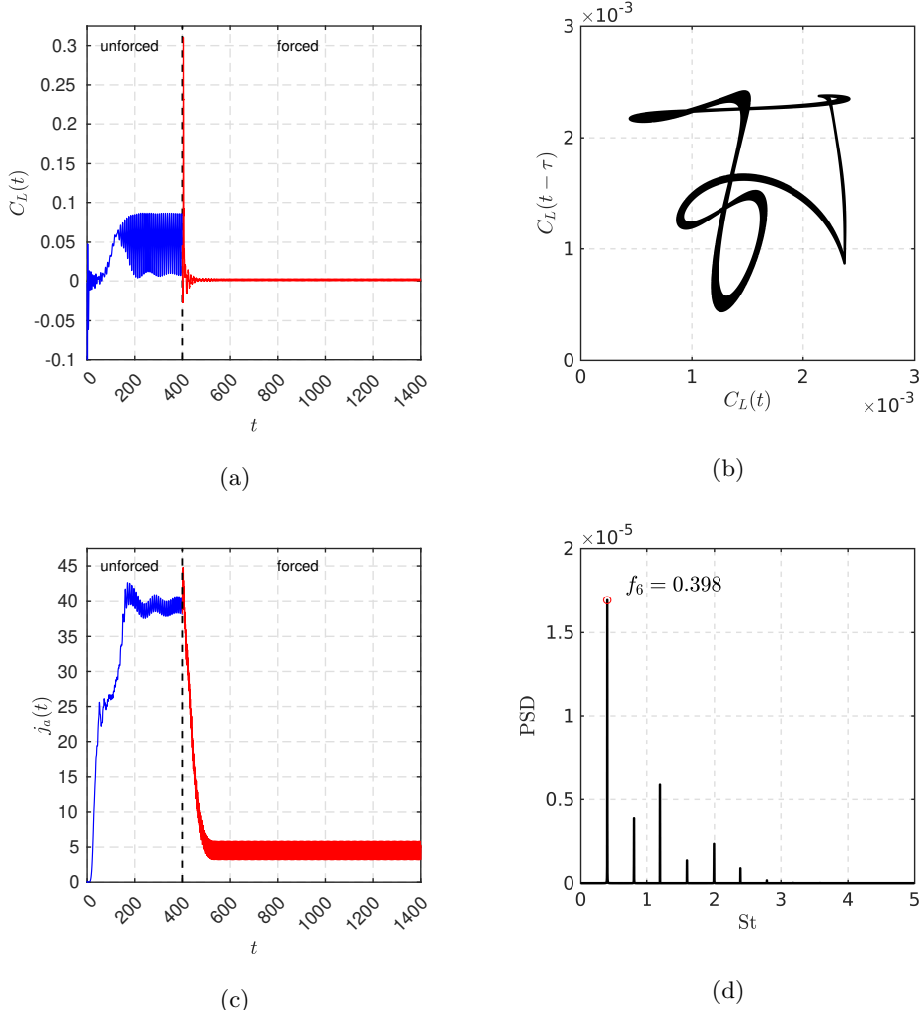


Figure 21: Characteristics of the best periodic forcing found with EGM. (a) Time evolution of the lift coefficient C_L , (b) phase portrait (c) time evolution of instantaneous cost function j_a and (d) Power Spectral Density (PSD) showing the main frequency $f_6 = 0.398$ of the forced flow and six harmonics. The control starts at $t = 400$. The unforced phase is depicted in blue and the forced one in red. The phase portrait and the PSD are computed over $t \in [900, 1400]$, during the post-transient regime.

REFERENCES

- BARROS, D., BORÉE, J., NOACK, B. R., SPOHN, A. & RUIZ, T. 2016 Bluff body drag manipulation using pulsed jets and Coanda effect. *J. Fluid Mech.* **805**, 442–459.
- BEARMAN, P. W. 1967 The effect of base bleed on the flow behind a two-dimensional model with a blunt trailing edge. *Aeronautical Quarterly* **18** (03), 207–224.
- BENARD, N., PONS-PRATS, J., PERIAUX, J., BUGEDA, G., BRAUD, P., BONNET, J.P. & MOREAU, E. 2016 Turbulent separated shear flow control by surface plasma actuator: experimental optimization by genetic algorithm approach. *Exp. Fluids* **57** (2), 22:1–17.
- BRAMEIER, M. & BANZHAF, W. 2006 *Linear Genetic Programming*. Springer Science & Business Media.

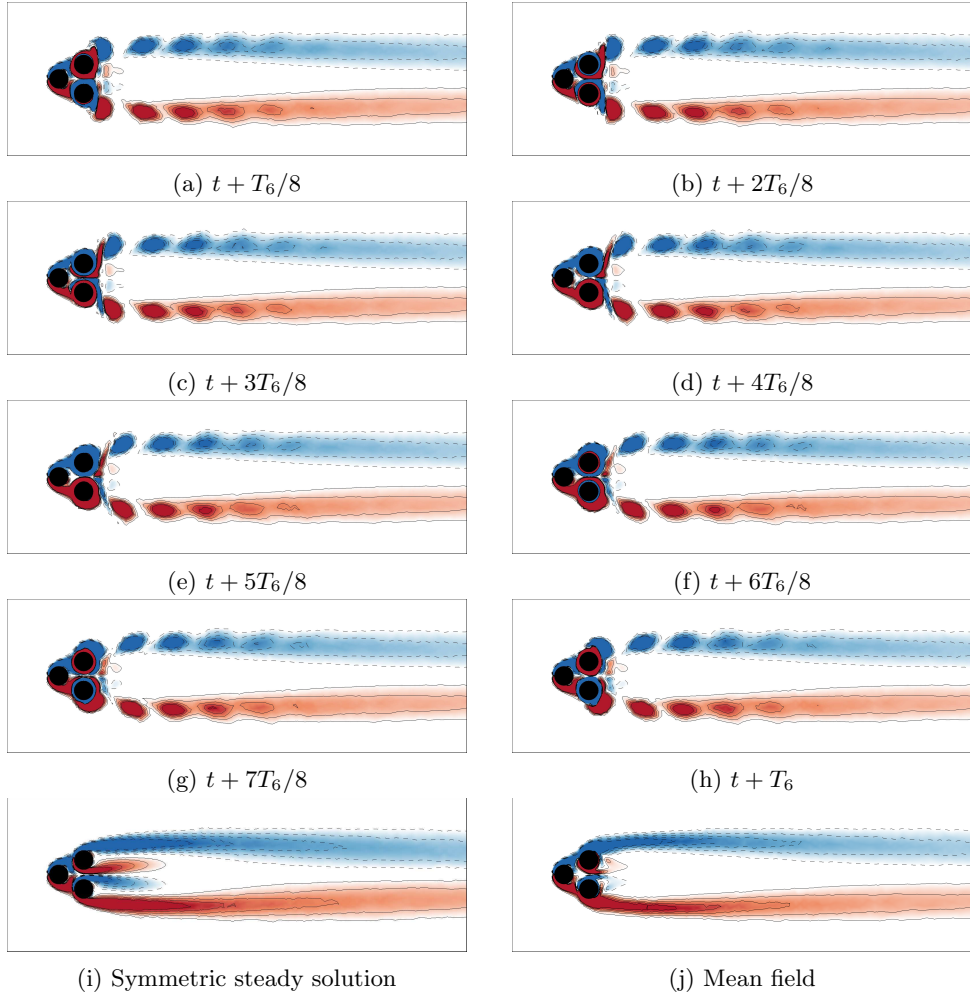


Figure 22: Vorticity fields of the best periodic forcing found with EGM. (a)-(f) Time evolution of the vorticity field throughout the last period of the 1400 convective time units, (i) the objective symmetric steady solution and (j) the mean field of the forced flow. The color code is the same as figure 1. T_6 is the period associated to the frequency f_6 . The mean field is computed by averaging 200 periods.

- BRUNTON, S. L. & NOACK, B. R. 2015 Closed-loop turbulence control: Progress and challenges. *Appl. Mech. Rev.* **67** (5), 050801:01–48.
- CATTAFFESTA, L. & SHELPACK, M. 2011 Actuators for active flow control. *Ann. Rev. Fluid Mech.* **43**, 247–272.
- CHEN, W., JI, C., ALAM, MD M., WILLIAMS, J. & XU, D. 2020 Numerical simulations of flow past three circular cylinders in equilateral-triangular arrangements. *J. Fluid Mech.* **891**, 1–44.
- CHOI, H., JEON, W. P. & KIM, J. 2008 Control of flow over a bluff body. *Ann. Rev. Fluid Mech.* **40**, 113–139.
- CHOI, H., MOIN, P. & KIM, J. 1994 Active turbulence control for drag reduction in wall-bounded flows. *J. Fluid Mech.* **262**, 75–110.
- CORNEJO MACEDA, G. Y., NOACK, B. R., LUSSEYRAN, F., DENG, N., PASTUR, L. &

- MORZYŃSKI, M. 2019 Artificial intelligence control applied to drag reduction of the fluidic pinball. *Proc. Appl. Math. Mech.* **19** (1), e201900268:1–2.
- CORTELEZZI, L., LEONARD, A. & DOYLE, J.C. 1994 An example of active circulation control of the unsteady separated flow past a semi-infinite plate. *J. Fluid Mech.* **260**, 127–154.
- DEBIEN, A., VON KRBEK, K. A. F. F., MAZELLIER, N., DURIEZ, T., CORDIER, L., NOACK, B. R., ABEL, M. W. & KOURTA, A. 2016 Closed-loop separation control over a sharp-edge ramp using genetic programming. *Exp. Fluids* **57** (3), 40:1–19.
- DENG, N., NOACK, B. R., MORZYŃSKI, M. & PASTUR, L. R. 2020 Low-order model for successive bifurcations of the fluidic pinball. *J. Fluid Mech.* **884**, A37.
- DOWLING, A. P. & MORGANS, A. S. 2005 Feedback control of combustion oscillations. *Annu. Rev. Fluid Mech.* **37** (151–182).
- DRACOPOULOS, D. C. 1997 *Evolutionary Learning Algorithms for Neural Adaptive Control*. London, etc.: Springer-Verlag.
- DURIEZ, T., BRUNTON, S. L. & NOACK, B. R. 2016 *Machine Learning Control — Taming Nonlinear Dynamics and Turbulence*, *Fluid Mech. its Appl.*, vol. 116. Springer-Verlag.
- FERNEX, D., SEMANN, R., ALBERS, M., MEYSONNAT, P. S., SCHRÖDER, W. & NOACK, B. R. 2020 Self-similar drag reduction formula from sparse data—Optimization of turbulent skin-friction via spanwise travelling surface waves. *Phys. Rev. Fluids* **5** (7), 073901:1–18.
- FLÜGEL, G. 1930 Ergebnisse aus dem Strömungsinstitut der Technischen Hochschule Danzig. In *Jahrbuch der Schiffbautechnischen Gesellschaft*, pp. 87–113. Springer.
- FUKAGATA, K. & NOBUHIDE, K. 2003 Drag reduction in turbulent pipe flow with feedback control applied partially to wall. *Int. J. Heat Fluid Flow* **24**, 480–490.
- GAUTIER, N., AIDER, J.-L., DURIEZ, T., NOACK, B. R., SEGOND, M. & ABEL, M. W. 2015 Closed-loop separation control using machine learning. *J. Fluid Mech.* **770**, 424–441.
- GELBERT, G., MOECK, J. P., PASCHEREIT, C. O. & KING, R. 2012 Advanced algorithms for gradient estimation in one-and two-parameter extremum seeking controllers. *J. Process Control* **22** (4), 700–709.
- GERHARD, J., PASTOOR, M., KING, R., NOACK, B. R., DILLMANN, A., MORZYŃSKI, M. & TADMOR, G. 2003 Model-based control of vortex shedding using low-dimensional Galerkin models. In *33rd AIAA Fluids Conference and Exhibit*. Orlando, Florida, USA, June 23–26, 2003, paper 2003-4262.
- GEROPP, D. 1995 Process and device for reducing the drag in the rear region of a vehicle, for example, a road or rail vehicle or the like. United States Patent **US 5407245 A**.
- GEROPP, D. & ODENTHAL, H.-J. 2000 Drag reduction of motor vehicles by active flow control using the Coanda effect. *Exp. Fluids* **28** (1), 74–85.
- GLEZER, A., AMITAY, M. & HONOHAN, A.M. 2005 Aspects of low- and high-frequency actuation for aerodynamic flow control. *AIAA Journal* **43** (7), 1501–1511.
- HERVÉ, A., SIPP, D., SCHMID, P. J. & SAMUELIDES, M. 2012 A physics-based approach to flow control using system identification. *J. Fluid Mech.* **702**, 26–58.
- ISHAR, R., KAISER, E., MORZYŃSKI, M., FERNEX, D., SEMAAN, R., ALBERS, M., MEYSONNAT, P. S., SCHRÖDER, W. & NOACK, BERND R. 2019 Metric for attractor overlap. *J. Fluid Mech.* **874**, 720–755.
- JORDAN, P. & COLONIUS, T. 2013 Wave packets and turbulent jet noise. *Ann. Rev. Fluid Mech.* **45**, 173–195.
- KOUOMOUTSAKOS, P., FREUND, J. & PAREKH, D. 2001 Evolution strategies for automatic optimization of jet mixing. *AIAA J.* **39** (5), 967–969.
- LI, H., FERNEX, D., TAN, J., MORZYŃSKI, M. & NOACK, B. R. 2020a Cluster-based network model. *J. Fluid Mech.* (**in print**, see arXiv **2001.02911**).
- LI, R., BORÉE, J., NOACK, B. R., CORDIER, L. & HARAMBAT, F. 2019 Drag reduction mechanisms of a car model at moderate yaw by bi-frequency forcing. *Phys. Rev. Fluids* **4** (3), 034604.
- LI, R., NOACK, B. R., CORDIER, L., BORÉE, J., KAISER, E. & HARAMBAT, F. 2018 Linear genetic programming control for strongly nonlinear dynamics with frequency crosstalk. *Archives of Mechanics* **70** (6), 505–534.
- LI, Y., CUI, W., JIA, Q., LI, Q., YANG, Z., MORZYŃSKI, M. & NOACK, B. R. 2020b Explorative gradient method for active drag reduction of the fluidic pinball and slanted ahmed body. *J. Fluid Mech.* (**submitted**, see arXiv **1905.12036v2**).

- LUCHTENBURG, D. M., GÜNTER, B., NOACK, B. R., KING, R. & TADMOR, G. 2009 A generalized mean-field model of the natural and actuated flows around a high-lift configuration. *J. Fluid Mech.* **623**, 283–316.
- MCKAY, M. D., BECKMAN, R. J. & CONOVER, W. J. 1979 A comparison of three methods for selecting values of input variables in the analysis of output from a computer code. *Technometrics* **21** (2), 239–245.
- NELDER, J. A. & MEAD, R. 1965 A simplex method for function minimization. *Computer Journal* **7** (4), 308–313.
- NOACK, B. R. 2019 Closed-loop turbulence control—From human to machine learning (and retour). In *Proceedings of the 4th Symposium on Fluid Structure-Sound Interactions and Control (FSSIC), Tokyo, Japan* (ed. Y. Zhou, M. Kimura, G. Peng, A. D. Lucey & L. Hung), pp. 23–32. Springer.
- NOACK, B. R., AFANASIEV, K., MORZYŃSKI, M., TADMOR, G. & THIELE, F. 2003 A hierarchy of low-dimensional models for the transient and post-transient cylinder wake. *J. Fluid Mech.* **497**, 335–363.
- NOACK, B. R., STANKIEWICZ, W., MORZYŃSKI, M. & SCHMID, P. J. 2016 Recursive dynamic mode decomposition of transient and post-transient wake flows. *J. Fluid Mech.* **809**, 843–872.
- PAREZANOVIĆ, V., CORDIER, L., SPOHN, A., DURIEZ, T., NOACK, B. R., BONNET, J.-P., SEGOND, M., ABEL, M. & BRUNTON, S. L. 2016 Frequency selection by feedback control in a turbulent shear flow. *J. Fluid Mech.* **797**, 247–283.
- PASTOOR, M., HENNING, L., NOACK, B. R., KING, R. & TADMOR, G. 2008 Feedback shear layer control for bluff body drag reduction. *J. Fluid Mech.* **608**, 161–196.
- PFEIFFER, J. & KING, R. 2012 Multivariable closed-loop flow control of drag and yaw moment for a 3d bluff body. In *6th AIAA Flow Control Conference*, pp. 1–14. Atlanta, Georgia, USA.
- PROTAS, B. 2004 Linear feedback stabilization of laminar vortex shedding based on a point vortex model. *Phys. Fluids* **16** (12), 4473–4488.
- RABAULT, J., KUCHTA, M., JENSEN, A., RÉGLADE, U. & CERARDI, N. 2019 Artificial neural networks trained through deep reinforcement learning discover control strategies for active flow control. *J. Fluid Mech.* **865**, 281–302.
- RAIBAUDET, C., ZHONG, P., NOACK, B. R. & MARTINUZZI, R. J. 2019 Machine learning strategies applied to the control of a fluidic pinball. *Phys. Fluids* **32**, 015108.
- REN, F., HU, H. B. & TANG, H. 2020 Active flow control using machine learning: A brief review. *J. Hydraul. Dyn.* **32** (2), 247–253.
- ROUSSOPOULOS, K. 1993 Feedback control of vortex shedding at low Reynolds numbers. *J. Fluid Mech.* **248**, 267–296.
- ROWAN, T. 1990 The subplex method for unconstrained optimization. PhD thesis, Department of Computer Sciences, University of Texas.
- ROWLEY, C. W. & WILLIAMS, D. R. 2006 Dynamics and control of high-Reynolds number flows over open cavities. *Ann. Rev. Fluid Mech.* **38**, 251–276.
- SEIFERT, J. 2012 A review of the Magnus effect in aeronautics. *Prog. Aerosp. Sci.* **55**, 17–45.
- SEMAAN, R., KUMAR, P., BURNAZZI, M., TISSOT, G., CORDIER, L. & NOACK, B. R. 2016 Reduced-order modeling of the flow around a high-lift configuration with unsteady Coanda blowing. *J. Fluid Mech.* **800**, 71–110.
- THIRIA, B., GOUPON-DURAND, S. & WESFREID, J. E. 2006 The wake of a cylinder performing rotary oscillations. *J. Fluid Mech.* **560**, 123–147.
- WOOD, C. J. 1964 The effect of base bleed on a periodic wake. *J. R. Soc. Interface* **68** (643), 477–482.
- ZHOU, Y., FAN, D., ZHANG, B., LI, R. & NOACK, B. R. 2020 Artificial intelligence control of a turbulent jet. *J. Fluid Mech.* **897**, 1–46.